Linear instabilities of pulsatile plane channel flow between compliant walls

Smail Lebbal, Frédéric Alizard, Benoît Pier

Linear instabilities of pulsatile plane channel flow between compliant walls

Smail Lebbal, Frédéric Alizard and Benoît Pier†

Laboratoire de mécanique des fluides et d'acoustique,
CNRS, École centrale de Lyon, Université de Lyon 1, INSA Lyon,
36 avenue Guy-de-Collongue, 69134 Écully, France

(6 February 2022)

The linear dynamics of perturbations developing in a channel with compliant walls is investigated for pulsatile base flows. It is found that the flow dynamics is mainly governed by four control parameters: the Reynolds number Re, the reduced velocity V_R, the Womersley number Wo and the amplitude of the base flow modulation $\widetilde{Q}$. Linear stability analyses are carried out within the framework of Floquet theory, implementing an efficient approach for removing spurious eigenmodes. The characteristics of flow-based (Tollmien–Schlichting) and wall-based (both travelling-wave flutter and divergence) modes are investigated over a large control-parameter space. It is shown that travelling-wave flutter (TWF) modes are predominantly influenced by the reduced velocity and that the Reynolds number has only a marginal effect. The critical reduced velocity (corresponding to onset of linear instability) is demonstrated to depend both on the Womersley number and modulation amplitude for a given set of wall parameters. The Tollmien–Schlichting (TS) mode is only weakly affected by the flexibility of the wall. Finally, the classification given by Benjamin (*J. Fluid Mech.* **16** 436–450, 1963) is found to be too restrictive in the case of pulsatile base flows. In particular, a new type of transition mode is identified that results from the coalescence of two Floquet eigenmodes: interaction between TS and TWF modes due to coupling of the different Floquet harmonics, a phenomenon specific to time-periodic base flows.

Key words: Fluid–structure interactions, instability, Floquet theory

1. Introduction

Pulsating flows in pipe or channel flows are laminar provided that Reynolds numbers are sufficiently low as is largely the case for vast parts of the caridovascular system. In the main arteries, however, blood flow may experience instability waves, generating large fluctuating shear stresses, which are a possible cause for cardiovascular diseases (Chiu & Chien 2011). The compliance of arteries plays a major role in blood transport, such as maintaining blood pressure and regularizing the flow rate (Ku 1997). The flexibility of the aorta is also a key element in minimizing pressure fluctuations of blood provided by the left ventricle

† Email address for correspondence: benoit.pier@cnrs.fr.

and distributing oxygen-rich blood through capillaries (O'Rourke & Hashimoto 2007). For these reasons, both flexible walls and pulsatile flow are ubiquitous in the physiological context. When a pulsatile flow interacts with compliant walls, a better understanding of the development of instabilities is therefore required in order to improve the analysis of the link between wall-shear stress distributions and flow dynamics.

The theory of viscous flow interacting with compliant walls has come a long way from Gray (1936)'s initial observations of the outstanding performance of dolphin skins in delaying turbulence, to the recent review of Kumaran (2021) enlightening the various instability mechanisms. In the 50s, Kramer conducted pioneering tests in water by towing a dolphin-shaped object covered with viscoelastic materials of varying compliance (Kramer 1957). The author shows that the compliant coating leads to a significant drag reduction and suggests that the dolphin's secret originates in the laminarisation of the flow due to its skin material.

On one hand, several researchers tried and failed to replicate Kramer's experiments; see Gad-el-Hak (1986, 1996) for reviews. On the other hand, theoretical results of Carpenter & Garrad (1985) extend the first analytical studies developed by Benjamin (1959, 1960, 1963) and Landahl (1962) and demonstrate that a suitable choice of wall properties could control the onset of the primary instability mode of a flat-plate boundary layer, the so-called Tollmien–Schlichting (TS) mode. However, it is also suggested that the emergence of solid-based instability modes due to fluid–structure interactions (also referenced as flow–structure instabilities, FSI) can limit the potential of laminarisation of the flow (Carpenter & Garrad 1986). The FSI modes can be divided into two categories: the travelling-wave flutter (TWF) modes and the (almost static) divergence (DIV) modes. While the physics of TWF modes is fairly well understood using an analogy with the onset of water-waves (Miles 1957), scientists are still arguing about the physical mechanism behind the divergence mode. The first successful experimental attempt to reproduce Kramer's findings was given by Gaster (1988). In particular, he found that the measured growth rates of TS waves developing along a simple compliant coating match those obtained by Carpenter & Garrad (1985).

Several attempts to classify instability modes in the presence of fluid–structure interactions were made since the seminal study of Benjamin (1963). In particular, three types of instability mechanisms have been considered: TS modes belong to class A, TWF modes are associated with class B and class C modes correspond to almost steady waves, i.e. the divergence mode (see Davies & Carpenter (1997*a*,*b*) for the channel flow case). Apart from these modes, a transition mode is also found by Sen & Arora (1988), resulting from the coalescence between a TS mode and a TWF mode. For instance, Davies & Carpenter (1997*a*) have shown that the transition mode could develop inside a flow between a compliant channel for a sufficiently high level of wall damping. For the same flow case, we have recently shown that while class B modes are mainly driven by the reduced velocity, which corresponds to the ratio of characteristic wall and advection time scales, class C mode is influenced by both the Reynolds number and the reduced velocity (Lebbal *et al.* 2022).

Independently of studies assessing optimal properties of wall coating to delay transition to turbulence in wall-bounded flows, the stability of pulsatile flow with respect to viscous shear instability modes has been theoretically addressed since the middle of the 70s (Davis 1976). In comparison with steady flows, pulsatile flows are governed by additional control parameters: the pulsation amplitudes and the pulsating frequency, of which the Womersley number Wo is a non-dimensional measure (see its definition in (3.6) below). In physiological situations, typical Womersley numbers for large blood vessels are in the range 5–15 (Ku 1997). Within a Floquet theory framework, von Kerczek (1982) shows that the sinusoidally pulsating flow developing between two flat plates is more stable than the steady plane Poiseuille flow for Womersley numbers in excess of Wo = 12. This result was confirmed by direct numerical simulations carried out by Singer *et al.* (1989). Using linear Floquet stability analyses and

nonlinear numerical simulations, Pier & Schmid (2017) explored a large parameter space for the same flow configuration, confirming and extending the earlier results given by von Kerczek (1982).

On the other hand, several authors (Straatman *et al.* 2002; Blennerhassett & Bassom 2006) have found that the perturbations may experience a strong increase in kinetic energy during the deceleration phase of the pulsatile base flow. This suggests that transient growth mechanisms and nonlinear effects come likely into play during this part of the pulsation cycle and that the flow could possibly break down to turbulence. Recently such a scenario has been further supported by nonmodal stability analyses, experiments and direct numerical simulations for both pipe and channel flows (Xu *et al.* 2020, 2021; Pier & Schmid 2021).

In spite of major successes achieved so far in the understanding of the dynamics prevailing for either pulsatile base flows or wall flexibility, only few studies address these two effects in combination. For the channel flow case, using Floquet stability analyses, Tsigklifis & Lucey (2017) show that wall flexibility has a stabilising effect for some range of the Womersley number. The combined effect of wall damping and Womersley number is also illustrated by these authors. However, the influence of the reduced velocity on travelling-wave flutter modes is not considered when the pulsatile base-flow component comes into play. Furthermore, it is not completely clear if the classification made by Benjamin (1963) still holds for the pulsatile flow case. Finally, the transition mode that emerges due to an increase in wall damping is not investigated when considering a pulsatile flow component.

To provide further understanding to the above points, the present study addresses the linear stability properties of small-amplitude perturbations developing in pulsatile flows through compliant channels. This paper is organized as follows. In the section 2, we introduce the coupled fluid–structure system, and the base flow and non-dimensional control parameters are given in section 3. The mathematical formulation of the linear stability problem is presented in section 4. The numerical methods to solve and reduce the generalised eigenvalue problem are explainted in section 5. Section 6 devoted to the results constitutes the main contribution of the paper: discussion of the spectra, influence of the control parameters, spatio-temporal structure of the eigenmodes, and a variety of critical curves associated with onset of linear instability.

2. Fluid–structure interaction model and interface conditions.

In the present study, the analysis is restricted to the two-dimensional case. We introduce the Cartesian coordinate system (x, y) with unit vectors $(\mathbf{e_x}, \mathbf{e_y})$ and consider an incompressible Newtonian fluid with dynamic viscosity μ and density ρ between two spring-backed deformable plates located at $y = \zeta^{\pm}(x, t)$ which are allowed to move only in the wall-normal direction (see figure 1). The flow between the walls is governed by the Navier–Stokes equations

$$\rho \frac{\partial \mathbf{u}}{\partial t} + \rho(\mathbf{u} \cdot \nabla)\mathbf{u} = -\nabla p + \mu \Delta \mathbf{u}, \tag{2.1}$$

$$0 = \nabla \cdot \mathbf{u}, \tag{2.2}$$

where $\mathbf{u} = (u, v)$ is the velocity field, with streamwise (u) and wall-normal (v) velocity components, respectively, and p the pressure field.

The movement of the flexible plates obeys the following equations:

$$m \frac{\partial^2 \zeta^{\pm}}{\partial t^2} + d \frac{\partial \zeta^{\pm}}{\partial t} + \left(B \frac{\partial^4}{\partial x^4} - T \frac{\partial^2}{\partial x^2} + K \right) \zeta^{\pm} = f^{\pm}, \tag{2.3}$$

where m denotes the mass per unit area of the plates, d their damping coefficient, B the

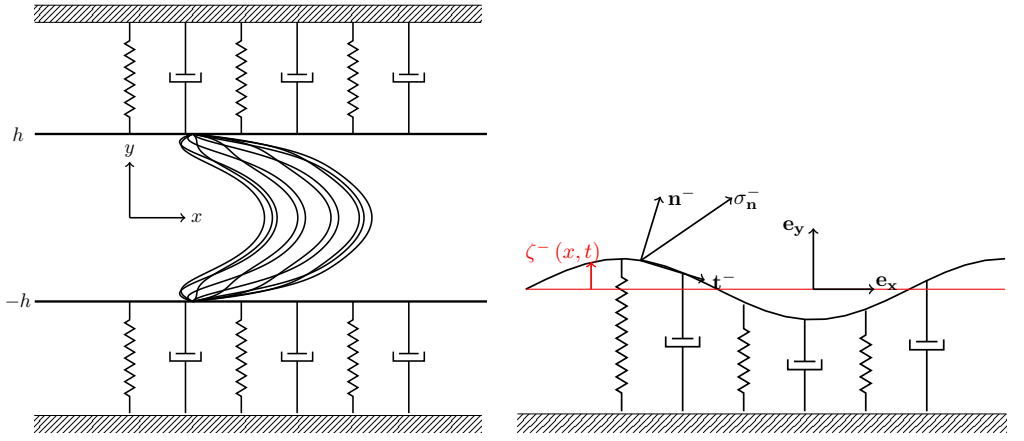

(a) Schematic diagram showing the equilibrium state configuration.

(b) Wall deformation and coordinates system.

Figure 1: Channel flow with infinite spring-backed flexible walls.

flexural rigidity, T the wall tension, K the spring stiffness and $f^{\pm}$ represents the y-component of the hydrodynamic forces acting on the plates. These forces are obtained as

$$f^{\pm} = \mathbf{e_y} \cdot \mathbf{f}^{\pm} \quad \text{with} \quad \mathbf{f}^{\pm} = \left(\overline{\overline{\tau}}^{\pm} - \delta p^{\pm}\mathbf{I}\right) \cdot \mathbf{n}^{\pm}. \tag{2.4}$$

Here $\overline{\overline{\tau}}^{\pm}$ denotes the viscous stress tensor at the walls, $\delta p^{\pm}$ the transmural surface pressure and $\mathbf{n}^{\pm} = \left(n_x^{\pm}, n_y^{\pm}\right)$ is the unit vector normal to the walls pointing towards the fluid. The y-component of the normal forces acting on the plate then reads

$$f^{\pm} = \mu\left(\left.\frac{\partial u}{\partial y}\right|_{y=\zeta^{\pm}} + \left.\frac{\partial v}{\partial x}\right|_{y=\zeta^{\pm}}\right) n_x^{\pm} + 2\mu \left.\frac{\partial v}{\partial y}\right|_{y=\zeta^{\pm}} n_y^{\pm} - \delta p^{\pm} n_y^{\pm}, \tag{2.5}$$

with

$$n_x^{\pm} = \pm \frac{\partial \zeta^{\pm}}{\partial x} \frac{1}{\sqrt{1 + \left(\frac{\partial \zeta^{\pm}}{\partial x}\right)^2}} \quad \text{and} \quad n_y^{\pm} = \mp \frac{1}{\sqrt{1 + \left(\frac{\partial \zeta^{\pm}}{\partial x}\right)^2}}. \tag{2.6}$$

Finally, the no-slip conditions on both walls lead to the kinematic conditions:

$$u = 0 \quad \text{and} \quad v = \frac{\partial \zeta^{\pm}}{\partial t} \quad \text{for} \quad y = \zeta^{\pm}. \tag{2.7}$$

The fluid–structure interaction problem is thus fully defined by the coupling of the fluid equations (2.1,2.2), the wall equations (2.3,2.5) and the boundary conditions (2.7).

3. Base flows and non-dimensional control parameters

A pulsatile base flow, of frequency Ω, is considered. Such a flow is driven by a spatially uniform and temporally periodic streamwise pressure gradient and is obtained as an exact solution of the Navier–Stokes equations. The solution consists of a velocity field in the streamwise direction with profiles that only depend on the wall-normal coordinate and time.

It can be expanded as a temporal Fourier series

$$\mathbf{U}(y,t) = U(y,t)\mathbf{e_x} \quad \text{with} \quad U(y,t) = \sum_n U^{(n)}(y)\exp(in\Omega t). \tag{3.1}$$

Similarly, the pressure gradient that drives the flow is expanded as

$$G(t) = \sum_n G^{(n)}\exp(in\Omega t) \tag{3.2}$$

and is associated with a pulsatile flow rate

$$Q(t) = \sum_n Q^{(n)}\exp(in\Omega t). \tag{3.3}$$

The velocity profile is analytically obtained for each harmonic component. The mean-flow component $U^{(0)}(y)$ corresponds to a parabolic steady Poiseuille flow solution. For $n \neq 0$, the profiles $U^{(n)}(y)$ are obtained in terms of exponential functions (Womersley 1955). Analytical expressions are detailed in the appendix of Pier & Schmid (2021). In this work, we focus on pulsatile base flows with a single oscillating component. We can thus write the flow rate as:

$$Q(t) = Q^{(0)}\left(1 + \widetilde{Q}\cos\Omega t\right), \tag{3.4}$$

with the relative pulsating amplitude $\widetilde{Q}$ defined as

$$\widetilde{Q} = 2\frac{Q^{(1)}}{Q^{(0)}}. \tag{3.5}$$

The problem is then characterized by 11 dimensional parameters: the mean flow rate $[Q^{(0)}] = \mathrm{m^3 s^{-1}}$, the half-channel width $[h] = \mathrm{m}$, the fluid density $[\rho] = \mathrm{kg\,m^{-3}}$, the viscosity $[\mu] = \mathrm{kg\,s^{-1}\,m^{-1}}$, the mass of the plate per unit area $[m] = \mathrm{kg\,m^{-2}}$, the damping coefficient of the wall $[d] = \mathrm{kg\,m^{-2}s^{-1}}$, the bending stiffness of the plate $[B] = \mathrm{kg\,m^2 s^{-2}}$, the wall tension $[T] = \mathrm{kg\,s^{-2}}$, the spring stiffness $[K] = \mathrm{kg\,m^{-2}s^{-2}}$, the pulsation frequency $[\Omega] = \mathrm{s^{-1}}$ and the amplitude of the oscillating flow component $[Q^{(1)}] = \mathrm{m^3 s^{-1}}$. Hence, the present configuration may be described by 8 non-dimensional control parameters.

The base flow is characterized by three non-dimensional parameters:

$$\mathrm{Re} = \frac{Q^{(0)}}{\nu}, \quad \mathrm{Wo} = h\sqrt{\frac{\Omega}{\nu}} \quad \text{and} \quad \widetilde{Q} = 2\frac{Q^{(1)}}{Q^{(0)}}. \tag{3.6}$$

Here, the Reynolds number Re is based on the average fluid velocity, the channel diameter and the kinematic viscosity $\nu = \mu/\rho$; the Womersley number Wo is a measure of the pulsation frequency and can be interpreted as the ratio of the channel half-diameter to the thickness $\delta = \sqrt{\nu/\Omega}$ of the oscillating Stokes boundary layers.

The parameters associated with the walls are non-dimensionalised with respect to the spring stiffness K, which leads to

$$B_* = \frac{B}{Kh^4}, \quad T_* = \frac{T}{Kh^2} \quad \text{and} \quad d_* = \frac{d}{\sqrt{mK}}. \tag{3.7}$$

Finally, two non-dimensional parameters account for the coupling between the fluid and the compliant walls

$$V_R = \frac{Q^{(0)}}{4h^2}\sqrt{\frac{m}{K}} \quad \text{and} \quad \Gamma = \frac{m}{\rho h}. \tag{3.8}$$

The reduced velocity V_R represents the ratio of the wall characteristic time scale $\tau_K = \sqrt{\frac{m}{K}}$,

associated with the spring stiffness, to the characteristic flow advection time scale $\tau_Q = \frac{4h^2}{Q^{(0)}}$ (de Langre 2000). The parameter Γ is the mass ratio between the walls and the fluid.

Unperturbed base configurations are thus completely specified by the 8 non-dimensional control parameters (3.6–3.8). We further use $\rho = 1$, $h = 1$ and $Q^{(0)} = 1$ to uniquely determine dimensional quantities. Hereafter, to reduce the dimensionality of control-parameter space, the mass ratio is kept constant at $\Gamma = 2$ and we consider walls without tension $T = 0$.

4. Linear stability analysis

For the stability analysis, the total flow fields are decomposed as the superposition of base and small-amplitude perturbation fields:

$$\mathbf{u}(x, y, t) = \mathbf{U}(y, t) + \mathbf{u}'(x, y, t), \tag{4.1}$$

$$p(x, y, t) = G(t)x + p'(x, y, t)\,. \tag{4.2}$$

The wall displacement is similarly written as

$$\zeta^{\pm}(x, t) = \pm h + \eta^{\pm\prime}(x, t). \tag{4.3}$$

Since the base configuration is homogeneous in x, perturbation fields may be expressed as spatial normal modes

$$\mathbf{u}'(x, y, t) = \tilde{\mathbf{u}}(y, t)e^{i\alpha x} + c.c., \tag{4.4}$$

$$p'(x, y, t) = \tilde{p}(y, t)e^{i\alpha x} + c.c., \tag{4.5}$$

$$\eta^{\pm\prime}(x, t) = \tilde{\eta}^{\pm}(t)e^{i\alpha x} + c.c., \tag{4.6}$$

where α denotes the streamwise wave number and $c.c.$ stands for the complex conjugate. Introducing this decomposition into the governing equations (2.1–2.3) and neglecting the quadratic terms leads to the following system of coupled linear partial differential equations:

$$\frac{\partial \tilde{u}}{\partial t} = -i\alpha U\,(y, t)\,\tilde{u} - \frac{\partial U}{\partial y}\,(y, t)\,\tilde{v} - \frac{1}{\rho} i\alpha\tilde{p} + \nu\left(\frac{\partial^2}{\partial y^2} - \alpha^2\right)\tilde{u}, \tag{4.7}$$

$$\frac{\partial \tilde{v}}{\partial t} = -i\alpha U\,(y, t)\,\tilde{v} \qquad - \frac{1}{\rho}\frac{\partial \tilde{p}}{\partial y} + \nu\left(\frac{\partial^2}{\partial y^2} - \alpha^2\right)\tilde{v}, \tag{4.8}$$

$$0 = i\alpha\tilde{u} + \frac{\partial \tilde{v}}{\partial y}, \tag{4.9}$$

$$m\frac{\partial \tilde{\gamma}^{\pm}}{\partial t} = -d\tilde{\gamma}^{\pm} - \left(B\alpha^4 + T\alpha^2 + K\right)\tilde{\eta}^{\pm} \pm \tilde{p}(y, t)\Big|_{\pm h} \mp \mu\frac{d\tilde{v}}{dy}\Big|_{\pm h}, \tag{4.10}$$

where we have introduced the additional functions $\tilde{\gamma}^{\pm} = \partial_t\tilde{\eta}^{\pm}$ in order to reduce the system to first-order differential equations in time. Note that the wall equations (4.10) assume a pressure outside the channel walls always equal to the unperturbed pressure $G(t)x$ prevailing inside (see Lebbal *et al.* (2022) for further details). The boundary conditions at the perturbed interface are expanded in a Taylor series about their equilibrium values at $y = \pm h$ (Shankar & Kumaran 2002). At linear order, the flow velocities at the walls are obtained as

$$\mathbf{u}\left(x, y = \zeta^{\pm}, t\right) = \mathbf{u}'\left(x, y = \pm h, t\right) + \eta^{\pm\prime}(x, t)\frac{dU}{dy}\Big|_{(y=\pm h,t)}\mathbf{e_x}. \tag{4.11}$$

Thus, the kinematic boundary conditions (2.7) become

$$\tilde{u}(y = \pm h, t) + \tilde{\eta}^{\pm}(t)\frac{dU}{dy}\Big|_{(y=\pm h,t)} = 0 \quad \text{and} \quad \tilde{v}(y = \pm h, t) = \tilde{\gamma}^{\pm}(t). \tag{4.12}$$

Since the base flow is time-periodic, the linear stability analysis proceeds by following Floquet theory, where the eigenfunctions are assumed to have the same temporal periodicity as the base flow. The perturbations are therefore further decomposed as

$$\tilde{\mathbf{u}}(y,t) = \left[\sum_n \hat{\mathbf{u}}^{(n)}(y)\exp\left(in\Omega t\right)\right]\exp\left(-i\omega t\right), \tag{4.13}$$

$$\tilde{p}(y,t) = \left[\sum_n \hat{p}^{(n)}(y)\exp\left(in\Omega t\right)\right]\exp\left(-i\omega t\right), \tag{4.14}$$

$$\tilde{\eta}^{\pm}(t) = \left[\sum_n \hat{\eta}^{\pm(n)}\exp\left(in\Omega t\right)\right]\exp\left(-i\omega t\right), \tag{4.15}$$

$$\tilde{\gamma}^{\pm}(t) = \left[\sum_n \hat{\gamma}^{\pm(n)}\exp\left(in\Omega t\right)\right]\exp\left(-i\omega t\right), \tag{4.16}$$

where the complex frequency $\omega = \omega_r + i\omega_i$ is the eigenvalue, with ω_i the growth rate and ω_r the circular frequency. After substitution of these expansions, the linearized equations governing the dynamics of small perturbations take the following form, for each integer n,

$$\begin{aligned}\omega\hat{u}^{(n)}(y) = &\left[n\Omega + i\nu\left(\partial_{yy} - \alpha^2\right)\right]\hat{u}^{(n)}(y) + \frac{\alpha}{\rho}\hat{p}^{(n)}(y)\\ &+ \sum_k\left[\alpha U^{(k)}(y)\hat{u}^{(n-k)}(y) - i\frac{dU^{(k)}}{dy}\hat{v}^{(n-k)}(y)\right],\end{aligned} \tag{4.17}$$

$$\begin{aligned}\omega\hat{v}^{(n)}(y) = &\left[n\Omega + i\nu\left(\partial_{yy} - \alpha^2\right)\right]\hat{v}^{(n)}(y) + \frac{1}{\rho}\frac{d\hat{p}^{(n)}}{dy}\\ &+ \sum_k\left[\alpha U^{(k)}(y)\hat{v}^{(n-k)}(y)\right],\end{aligned} \tag{4.18}$$

$$0 = i\alpha\hat{u}^{(n)}(y) + \frac{\partial\hat{v}^{(n)}}{\partial y}, \tag{4.19}$$

$$\omega\hat{\eta}^{\pm(n)} = n\Omega\hat{\eta}^{\pm(n)} + i\hat{\gamma}^{\pm(n)}, \tag{4.20}$$

$$\begin{aligned}\omega\hat{\gamma}^{\pm(n)} = &\, n\Omega\hat{\gamma}^{\pm(n)} - i\frac{d}{m}\hat{\gamma}^{\pm(n)} - \frac{i}{m}\left(B\alpha^4 + T\alpha^2 + K\right)\hat{\eta}^{\pm(n)}\\ &\pm\frac{i}{m}\left(\hat{p}^{(n)}(\pm h) - \mu\frac{d\hat{v}^{(n)}}{dy}\bigg|_{\pm h}\right),\end{aligned} \tag{4.21}$$

together with the kinematic wall conditions

$$\hat{u}^{(n)}(\pm h) = -\sum_k \frac{dU^{(k)}}{dy}\bigg|_{\pm h}\hat{\eta}^{\pm(n-k)}, \tag{4.22}$$

$$\hat{v}^{(n)}(\pm h) = \hat{\gamma}^{\pm(n)}. \tag{4.23}$$

The system of coupled linear differential equations (4.17–4.21) with boundary conditions (4.22,4.23) forms the generalised eigenvalue problem that governs the dynamics of small-amplitude perturbations developing in this time-periodic fluid–structure interaction system.

5. Numerical methods

In this section, we outline the numerical strategy that has been implemented for solving the generalised Floquet eigenvalue problem derived in the previous section. The main objectives in this implementation are the elimination of spurious (nonphysical) eigenvalues and the reduction of the required computational efforts. To that purpose, we follow the general framework described by Manning *et al.* (2007).

The velocity and pressure components are discretized in the wall-normal direction using a Chebyshev collocation method. To suppress spurious pressure modes, we consider the $(\mathbb{P}_N, \mathbb{P}_{N-2})$-formulation where the pressure is approximated with a polynomial of degree $N-2$ while the velocity is discretized with a polynomial of degree N (Schumack *et al.* 1991; Boyd 2001; Peyret 2002). In classical fashion, velocity fields are therefore represented by their values over N Gauss–Lobatto collocation points spanning the entire channel diameter and including the boundary points, while the pressure fields use only the $N-2$ interior points. We note the vectors containing the unkown velocity and pressure components at the interior points for each Fourier mode:

$$\mathbf{V_I}^{(n)} = \left(\hat{u}_2^{(n)}, \ldots, \hat{u}_{N-1}^{(n)}, \hat{v}_2^{(n)}, \ldots, \hat{v}_{N-1}^{(n)}\right), \tag{5.1}$$

$$\mathbf{P_I}^{(n)} = \left(\hat{p}_2^{(n)}, \ldots, \hat{p}_{N-1}^{(n)}\right). \tag{5.2}$$

Similary, wall displacements and wall velocities are denoted by

$$\mathbf{W}^{(n)} = \left(\hat{\eta}_1^{(n)}, \hat{\eta}_N^{(n)}, \hat{\gamma}_1^{(n)}, \hat{\gamma}_N^{(n)}\right). \tag{5.3}$$

The kinematic conditions (4.22,4.23) may be used to express the velocity values at the boundaries in terms of the wall variables. As a consequence, the variables $\hat{u}_1^{(n)}$, $\hat{v}_1^{(n)}$, $\hat{u}_N^{(n)}$ and $\hat{v}_N^{(n)}$ may be directly eliminated from the problem together with the boundary conditions. Then, using

$$\hat{\mathbf{X}}^{(n)} = \left(\mathbf{V_I}^{(n)}, \mathbf{P_I}^{(n)}, \mathbf{W}^{(n)}\right) \tag{5.4}$$

for each harmonic of the Floquet eigenvector, the system (4.17–4.21) is recast as a generalised algebraic eigenvalue problem of the form

$$\hat{\mathbf{A}}^{(n)}\hat{\mathbf{X}}^{(n)} + \sum_k \hat{\mathbf{S}}^{(k)}\hat{\mathbf{X}}^{(n-k)} = i\omega\hat{\mathbf{B}}^{(n)}\hat{\mathbf{X}}^{(n)}. \tag{5.5}$$

Here, the square matrices $\hat{\mathbf{A}}^{(n)}$, $\hat{\mathbf{S}}^{(k)}$ and $\hat{\mathbf{B}}^{(n)}$ are of size $(3N-2)^2$ and may be written in bloc structure as

$$\hat{\mathbf{A}}^{(n)} = \begin{pmatrix} \hat{\mathbf{A}}_{\mathbf{VV}}^{(n)} & \hat{\mathbf{G}}_{\mathbf{V}} & \hat{\mathbf{A}}_{\mathbf{VW}} \\ \hat{\mathbf{D}}_{\mathbf{V}} & \mathbf{0} & \hat{\mathbf{D}}_{\mathbf{W}} \\ \hat{\mathbf{A}}_{\mathbf{WV}} & \hat{\mathbf{G}}_{\mathbf{W}} & \hat{\mathbf{A}}_{\mathbf{WW}}^{(n)} \end{pmatrix}, \quad \hat{\mathbf{S}}^{(k)} = \begin{pmatrix} \hat{\mathbf{S}}_{\mathbf{VV}}^{(k)} & \mathbf{0} & \hat{\mathbf{S}}_{\mathbf{VW}}^{(k)} \\ \mathbf{0} & \mathbf{0} & \mathbf{0} \\ \mathbf{0} & \mathbf{0} & \mathbf{0} \end{pmatrix} \quad \text{and} \quad \hat{\mathbf{B}}^{(n)} = \begin{pmatrix} \mathbb{I}_{\mathbf{VV}} & \mathbf{0} & \mathbf{0} \\ \mathbf{0} & \mathbf{0} & \mathbf{0} \\ \mathbf{0} & \mathbf{0} & \mathbb{I}_{\mathbf{WW}} \end{pmatrix}. \tag{5.6}$$

Their decomposition in terms of square blocs along the diagonal and rectangular blocs off diagonal reflects the structure of the vectors $\hat{\mathbf{X}}^{(n)}$ (5.4), with $2N-4$ variables for $\mathbf{V_I}^{(n)}$, $N-2$ variables for $\mathbf{P_I}^{(n)}$, and 4 variables for $\mathbf{W}^{(n)}$. In the above expressions, n may in theory take all integer values (positive and negative) but in practice the Fourier series are truncated at $|n| \leqslant N_f$ for some cut-off value N_f. Note also that the blocs for which the superscript (n) is not indicated in (5.6) do not depend on a specific harmonic and that the matrix $\hat{\mathbf{B}}^{(n)}$ only consists of two identity blocs. The matrices $\hat{\mathbf{S}}^{(k)}$ account for the advection terms due to the pulsating base flow component $U^{(k)}(y)$ and are responsible for the coupling of the

different Fourier components of the Floquet eigenfunctions. Since we consider pulsating flows with only a single oscillating component $U^{(\pm 1)}(y)$, only the matrices $\hat{\mathbf{S}}^{(k)}$ with $|k| \leqslant 1$ are here non zero. As a result, the eigenvalue problem (5.5) has bloc-tridiagonal structure, which allows the use of efficient solution methods such as a generalised form of the Thomas algorithm.

The next step consists in eliminating the pressure by using the discrete version of the divergence-free condition

$$\hat{\mathbf{D}}_{\mathbf{V}} \mathbf{V_I}^{(n)} + \hat{\mathbf{D}}_{\mathbf{W}} \mathbf{W}^{(n)} = \mathbf{0}. \tag{5.7}$$

Hence, applying this divergence operator to the parts of the algebraic system (5.5) corresponding to the momentum equations yields:

$$\begin{aligned} -\left(\hat{\mathbf{D}}_{\mathbf{V}}\hat{\mathbf{G}}_{\mathbf{V}} + \hat{\mathbf{D}}_{\mathbf{W}}\hat{\mathbf{G}}_{\mathbf{W}}\right)\mathbf{P}_{\mathbf{I}}^{(n)} &= \begin{pmatrix}\hat{\mathbf{D}}_{\mathbf{V}} & \hat{\mathbf{G}}_{\mathbf{V}}\end{pmatrix}\begin{pmatrix}\hat{\mathbf{A}}_{\mathbf{VV}}^{(n)} & \hat{\mathbf{A}}_{\mathbf{VW}} \\ \hat{\mathbf{A}}_{\mathbf{WV}} & \hat{\mathbf{A}}_{\mathbf{WW}}^{(n)}\end{pmatrix}\begin{pmatrix}\mathbf{V}_{\mathbf{I}}^{(n)} \\ \mathbf{W}^{(n)}\end{pmatrix} \\ &\quad + \hat{\mathbf{D}}_{\mathbf{V}} \sum_k \left(\hat{\mathbf{S}}_{\mathbf{VV}}^{(k)}\mathbf{V}_{\mathbf{I}}^{(n-k)} + \hat{\mathbf{S}}_{\mathbf{VW}}^{(k)}\mathbf{W}^{(n-k)}\right). \end{aligned} \tag{5.8}$$

The operator $(\hat{\mathbf{D}}_{\mathbf{V}}\hat{\mathbf{G}}_{\mathbf{V}} + \hat{\mathbf{D}}_{\mathbf{W}}\hat{\mathbf{G}}_{\mathbf{W}})$ is a square matrix of size $(N-2)^2$, independent of the harmonic n and non singular. By inverting it, the pressure components $\mathbf{P}_{\mathbf{I}}^{(n)}$ are obtained as the result of linear operators acting on the components $\mathbf{V}_{\mathbf{I}}^{(k)}$ and $\mathbf{W}^{(k)}$.

Thus eliminating the pressure, the system (5.5) is recast as

$$\mathbf{A}^{(n)}\mathbf{X}^{(n)} + \sum_k \mathbf{S}^{(k)}\mathbf{X}^{(n-k)} = i\omega\mathbf{X}^{(n)}. \tag{5.9}$$

Now, the components of the eigenvector

$$\mathbf{X}^{(n)} = \left(\mathbf{V_I}^{(n)}, \mathbf{W}^{(n)}\right) \tag{5.10}$$

contain $2N$ variables and the new matrices $\mathbf{A}^{(n)}$ and $\mathbf{S}^{(k)}$ are of size $(2N)^2$. Note also that, through the elimination of the pressure, the generalised eigenproblem (5.5) has been transformed into a regular eigenproblem.

The system (5.9) may be further reduced when $\alpha \neq 0$. Indeed, using the discretized version of the divergence-free condition $\tilde{u} = \frac{i}{\alpha}\partial_y \tilde{v}$, allows to eliminate the longitudinal velocity components by expressing them in terms of the wall-normal velocities. This leads to an eigenvalue problem of the same form as (5.9) where the components of the eigenvector are of size $N+2$, with $N-2$ wall-normal velocity values and 4 wall variables. In practice, this system is solved using an Arnoldi algorithm that exploits the bloc-tridiagonal structure of the matrices.

The transformations that have led from the initial generalised eigenvalue problem of size $3N+2$ to a regular eigenproblem of size $N+2$ may appear tedious. However, it is largely worth the effort: the final formulation is not only free of spurious eigenmodes, it is also drastically more efficient in terms of numerical computations. Finally, the method may be further improved by considering separately perturbations of sinuous or varicose symmetries and using only half of the channel together with derivative operators appropriate for the symmetry of each component of the different flow fields. Thus the complete problem may be addressed by carrying out two eigenvalue computations (sinuous and varicose) of half size, which further speeds up the process and directly provides the information about the symmetry of the different modes.

The numerical method has been validated using the results given by Pier & Schmid (2017)

for the pulsatile flow inside a rigid channel and those provided by Davies & Carpenter (1997*a*) for the steady base flow between compliant walls.

6. Stability analysis

In fluid–structure interaction problems, perturbations are classically identified as either fluid-based or solid-based instabilities, depending on the nature of the main driving mechanism. For steady flows in compliant channels, Tollmien–Schlichting (TS) modes are known as the prevailing fluid-based instabilities: they are driven by a viscous instability within the bulk of the flow and only weakly affected by wall compliance. On the other hand, solid-based instabilities are due to the interaction between a compliant wall and the fluid flow and are often labelled as fluid–structure interaction (FSI) modes since their dynamics is predominantly governed by the wall parameters. Among these FSI modes, one may further distinguish between travelling-wave flutter (TWF) and divergence (DIV) modes: while DIV modes are almost stationary, TWF modes display phase velocities of the same order as those of elastic waves due to the wall only. However, such a mode classification is not always possible since one type may continuously transform into another. For example, when the phase speed of TWF modes approaches that of TS modes, merging may occur to form a transition instability mode.

The purpose of the present study is to identify the main instability modes in the presence of a pulsating base flow and to document their dynamics for a wide range of flow and wall parameters. We first discuss how the eigenvalue spectra are modified due to the time-periodic flow component. Then, the influence of the main control parameters on the dominant modes is investigated, with special attention given to possible cross over between different mode types. Close monitoring of the spatial and temporal structure of the eigenfunctions reveals the rich dynamics of perturbations interacting with the pulsating flow and the compliant wall. Finally, the multi-dimensional parameter space is mapped out using a variety of critical curves for instability onset.

6.1. *The Floquet eigenspectrum*

The linear stability properties of time-periodic flow configurations is addressed by resorting to Floquet theory, as explained in section §4. In order to introduce the specific features of Floquet eigenspectra that are essential to this entire investigation, we illustrate them for a situation with small pulsation amplitude $\widetilde{Q}$, and compare them with the corresponding steady case.

Figure 2 shows the eigenvalue spectrum computed with $\alpha = 1$ for a pulsating base configuration characterized by $V_R = 1$, Wo = 10, $\widetilde{Q} = 0.02$, Re = 10000, $B_* = 4$ and $d_* = 0$. This plot reveals the characterisic feature of any Floquet spectrum: multiple eigenvalues of same growth rate ω_i and frequencies ω_r separated by integer multiples of the base frequency Ω. This is due to the fact that if ω is a complex eigenvalue associated with an eigenfunction of the form (4.13–4.16), then all frequencies $\omega_\star = \omega + k\Omega$ (for any positive or negative integer k) are also among the eigenvalues and their associated eigenfunctions are simply obtained by similarly shifting the Fourier components in the Floquet expansion as, for example, $\hat{\mathbf{u}}_\star^{(n)}(y) = \hat{\mathbf{u}}^{(n-k)}(y)$. In theory, the Fourier expansions (4.13–4.16) are infinite series, and the infinite number of eigenvalues $\omega + k\Omega$ correspond thus all to the same physical perturbation. In practice, however, the Fourier expansions are truncated to a finite number of components, leading to a finite set of eigenvalues $\omega_\star$. These are then no longer exactly equal to $\omega + k\Omega$ and the associated normal modes also differ since they correspond to different truncations of the Fourier series.

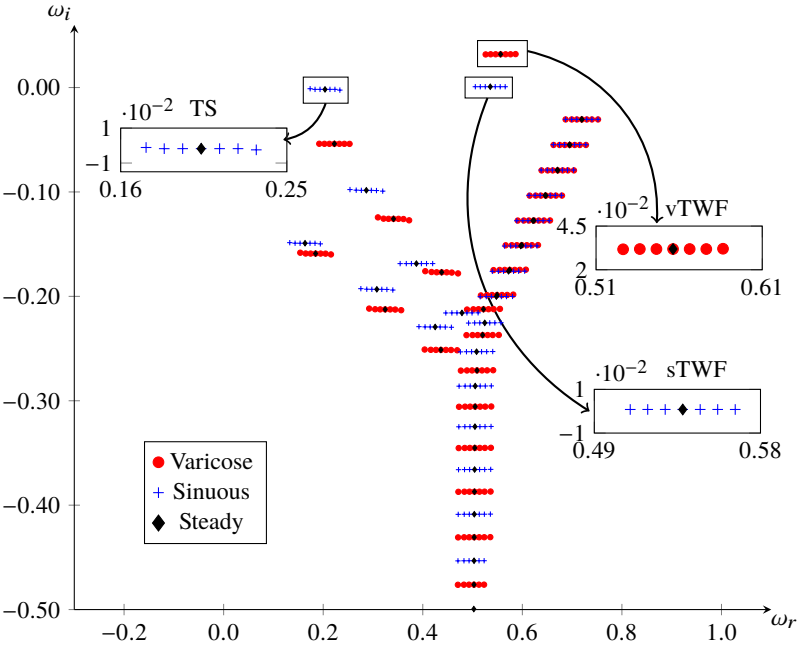

Figure 2: Spectrum for $\widetilde{Q} = 0.02$, Wo = 10, $V_R = 1$, Re = 10000, $\alpha = 1$, $B_* = 4$ and $d_* = 0$. The steady case corresponds to $\widetilde{Q} = 0$.

In figure 2, the Floquet eigenspectrum for $\widetilde{Q} = 0.02$ is shown together with the eigenspectrum of the corresponding steady configuration (at $\widetilde{Q} = 0$). This superposition illustrates the close similarity of both spectra and reveals that each of the steady eigenvalues is located very near one of the Floquet eigenvalues (see insets). Here, the Floquet spectrum corresponds to a weakly modulated base flow, for which the oscillating base-flow component $U^{(\pm 1)}(y)$ is much smaller than the Poiseuille component $U^{(0)}(y)$. Thus, the magnitude of the off-diagonal blocs $\mathbf{S}^{(\pm 1)}$ in the Floquet eigenproblem (5.9) is small in comparison with the diagonal blocs and the adjacent Fourier components in the Floquet eigenfunction are therefore only weakly coupled. As a result, the growth rates in the eigenspectrum here closely follow those prevailing for the equivalent steady flow. For weakly modulated base flows, as is the case in figure 2, it seems thus natural to choose the eigenvalue $\omega + k\Omega$ nearest its steady counterpart as the most representative frequency of the Floquet normal mode.

For larger pulsation amplitudes $\widetilde{Q}$, however, this similarity with the steady spectrum no longer holds and a more robust criterion is required to lift the formal degeneracy of the Floquet eigenspectrum. In order to identify the most representative frequency among the multiple Floquet eigenvalues for each normal mode, we consider the magnitude of the different Fourier components of the Floquet eigenfunctions, defined as

$$E_n = \rho \int_{-h}^{+h} |\hat{\mathbf{u}}^{(n)}(y)|^2 dy + m\left(|\hat{\gamma}^{+(n)}|^2 + |\hat{\gamma}^{-(n)}|^2\right) + \left(B\alpha^4 + T\alpha^2 + K\right)\left(|\hat{\eta}^{+(n)}|^2 + |\hat{\eta}^{-(n)}|^2\right). \quad (6.1)$$

By using this energy-based norm, it is possible to single out the dominant component in the eigenfunction Fourier expansion and also to check if the truncation contains enough harmonics for an accurate representation of the normal mode. This process is illustrated in

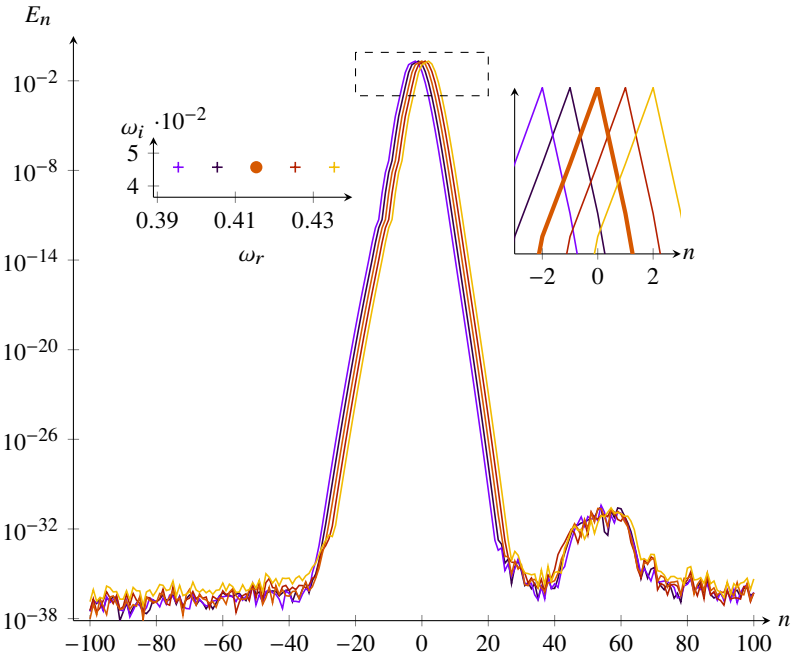

Figure 3: Fourier density for FSI varicose mode associated with $\alpha = 0.8$, Re = 10000, $\widetilde{Q} = 0.2$, Wo = 10, $V_R = 1$, $B_* = 4$ and $d_* = 0$.

figure 3, where the magnitudes E_n are plotted for five consecutive eigenvalues corresponding to the varicose TWF mode associated with $\alpha = 0.8$, Re = 10000, $\widetilde{Q} = 0.2$, Wo = 10, $V_R = 1$, $B_* = 4$ and $d_* = 0$. It is observed that the E_n-distribution peaks at $n = 0$ for the eigenvalue $\omega = 0.415+0.046\mathrm{i}$, while the distributions associated with the surrounding eigenfrequencies $\omega + k\Omega$ peak at $n = k$ since they correspond to similarly shifted Fourier components. It follows that $\omega = 0.415+0.046\mathrm{i}$ is the dominant frequency of this eigenmode. Throughout this paper we will therefore always consider that, for a given mode, the dominant frequency is derived by this energy-based criterion and choose the eigenvalue for which the Fourier series is centered on the $n = 0$ component, i.e. for wich E_0 is largest. For the rigid wall case, this method has been proven to be effective in recovering the TS mode frequency obtained using linearized direct numerical simulation (results are given in Pier & Schmid (2017)). Note also that the plots in figure (3) demonstrate that we are using more than enough harmonics to fully resolve the Floquet eigenfunctions.

The Floquet eigenfunctions correspond to either sinuous or varicose modes, depending on the symmetry or antisymmetry of the different flow fields with respect to the mid-plane $y = 0$. As explained in section §5, they may be efficiently computed by taking advantage of these symmetry properties. In the spectrum of figure 2, the sinuous eigenfrequencies are given in blue and the varicose frequencies in red. Despite the multiplicity of the eigenvalues due to the time-periodic base flow, the spectrum still displays the familiar structure made of a large number of Orr–Sommerfeld modes (as A, P and S branches) together with two isolated TWF modes (one sinuous and one varicose). Note that the two DIV modes are here out of the range of this plot.

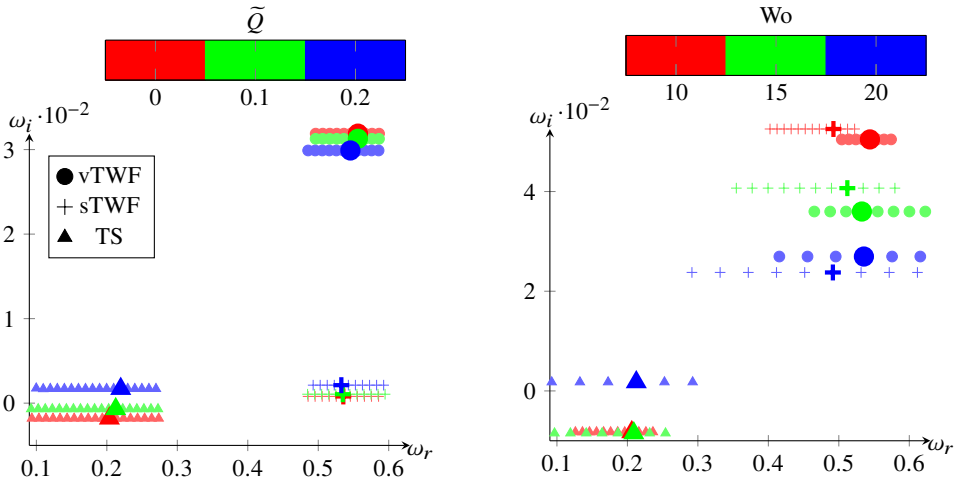

(a) Wo = 10. (b) $\widetilde{Q} = 0.8$.

Figure 4: Spectra with $V_R = 1$, Re = 10000, $\alpha = 1$, $B_* = 4$ and $d_* = 0$.

6.2. *Influence of some parameters on the spectrum*

The figure 4a displays spectra for $V_R = 1$, Wo = 10, $d_* = 0$ and $\widetilde{Q}$ varying from 0 (i.e. the steady flow case) to $\widetilde{Q} = 0.2$. The figure 4b illustrates the effect of the base-flow frequency by varying Wo from 10 to 20. As discussed in the previous section, the figure shows modes that exhibit equispaced eigenfrequencies where the gap between two successive frequencies corresponds to the base frequency Ω, which scales as the square root of the Wormersley number. In the figure 4, the bold eigenvalues are associated with the dominant frequency for each mode, obtained by considering the magnitude of the Floquet harmonics as explained in the previous subsection. Concentrating on FSI modes, dominant frequencies for both sinuous and varicose symmetries have finite ω_r values. These FSI modes are thus connected to TWF instability waves. They are referenced hereafter as sTWF (sinuous TWF) or vTWF (varicose TWF) depending on their symmetry with respect to the midplane $y = 0$.

For flow and wall parameters that are considered and $\widetilde{Q} = 0$, the most amplified TWF mode is of varicose type (see figure 4a). For this steady base flow case, the sTWF is seen to be marginally stable and the temporal growth rate of the TS mode is damped. For Wo = 10, an increase of $\widetilde{Q}$ tends to destabilise TS wave (see figure 4a). This is reminiscent of the results of Pier & Schmid (2017) where TS modes for a pulsatile base flow between rigid walls have been computed. By contrast, the TWF modes exhibit distinct behaviours whether the sinuous or varicose symmetry is considered. While an increase of $\widetilde{Q}$ leads to a reduction of the temporal amplification rate for the varicose type, the opposite behaviour is observed for the sinuous TWF mode. Figure 4b shows the effect of the Womersley number Wo onto TS and TWF modes for the same case. An increase of Wo has a stabilising effect on TWF modes for both symmetries. The opposite role of Wo is seen for the TS mode. This reflects the richness of physical processes that are involved, in comparison to the rigid wall case.

Finally, figure 5 shows the effect of wall compliance on TS and TWF modes for $\widetilde{Q} = 0.2$, Wo = 10, Re = 10000, $B_* = 4$ and $\alpha = 1$. Only Floquet modes that match the dominant frequency for each mode are shown. As V_R is approaching zero, the phase speed of TWF modes tends to infinity which is consistent with the rigid wall case. An increase of V_R has a stabilising effect on the TS mode. The opposite behaviour is observed for TWF modes whatever the symmetry considered. However, the figure suggests a preferred varicose

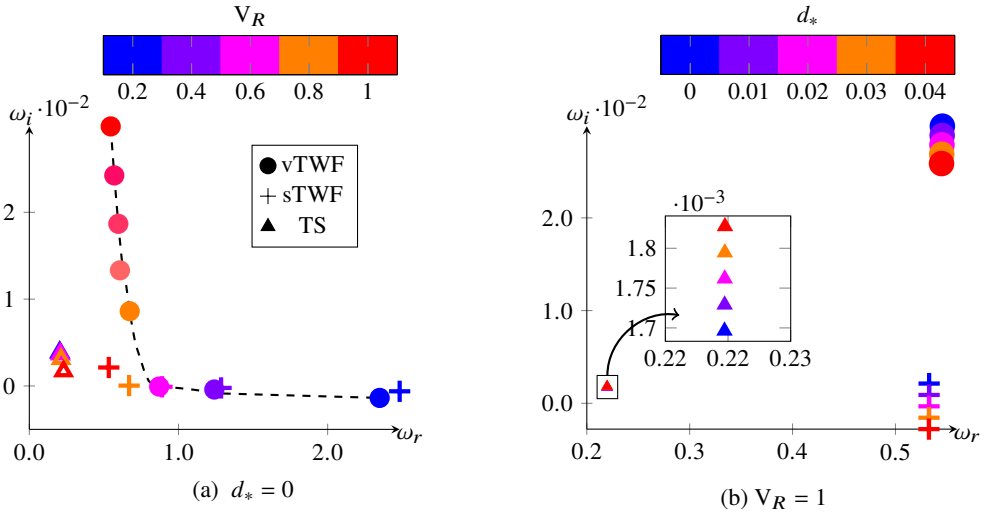

(a) $d_* = 0$ (b) $V_R = 1$

Figure 5: Spectra with $\widetilde{Q} = 0.2$, Wo = 10, Re = 10000, $\alpha = 1$ and $B_* = 4$.

symmetry for large V_R. Parenthetically, one can see in figure 5a that the phase speed tends to a finite value (≈ 0.5) for both sTWF and vTWF as wall compliance is increasing. The influence of the wall dissipation is illustrated in figure 5b for small values of d_*. The figure shows that the temporal amplification rate of the TS mode is slightly enhanced by increasing d_*. In contrast, growth rates of both sTWF and vTWF modes are significantly reduced by wall dissipation.

These behaviours suggest similarities between the steady case and our results. Especially, for the parameters that have been considered, the distinction made between class A and B modes by Benjamin (1963), Landahl (1962) and Carpenter & Garrad (1985) still holds for our pulsatile flow case. However, we will see in the next section that this classification is clearly too restrictive for pulsatile base flows.

6.3. *Waves superposition for sinuous Floquet mode*

The Fourier density distributions for a sinuous Floquet mode associated with $V_R = 1$, Wo = 10, Re = 10000, $\alpha = 1$, $B_* = 4$ and $d_* = 0$ are shown in figure 6 together with the associated eigenvalues for $\widetilde{Q} = 0.349$ and 0.350. Both series of eigenvalues have positive growth rates. The figure shows the existence of two distinct peaks in the Fourier density distribution. It suggests that two different mechanisms influence this mode. To further illustrate this scenario, the different contributions of the total energy per Fourier mode are also reported in figure 6. For the E_n-distribution at $\widetilde{Q} = 0.349$ (left curves), the main peak is due to the fluid kinetic energy contribution, associated with a dominant frequency of $\omega_r \simeq 0.26$. In contrast, for $\widetilde{Q} = 0.350$, the wall contributions take over, leading to a dominant frequency of $\omega_r \simeq 0.52$. For both cases, the E_n-distributions are very similar, but the exchange in dominant peaks due to a continuous modification of the distribution results in a sudden jump of the dominant frequency. This behaviour indicates that the intracyclic mechanism involves the interference between fluid-based (TS) and solid-based (TWF) modes. By contrast with the steady base flow case, we can therefore no longer distinguish here between class A and class B modes. Moreover, figure 6 also shows that for $\widetilde{Q} < 0.35$, the Floquet mode is mainly driven by its TS component. When $\widetilde{Q}$ is increased up to 0.35, the intracyclic growth is mainly due to its sTWF part. This new type of mode will be called hereafter a two-waves mode.

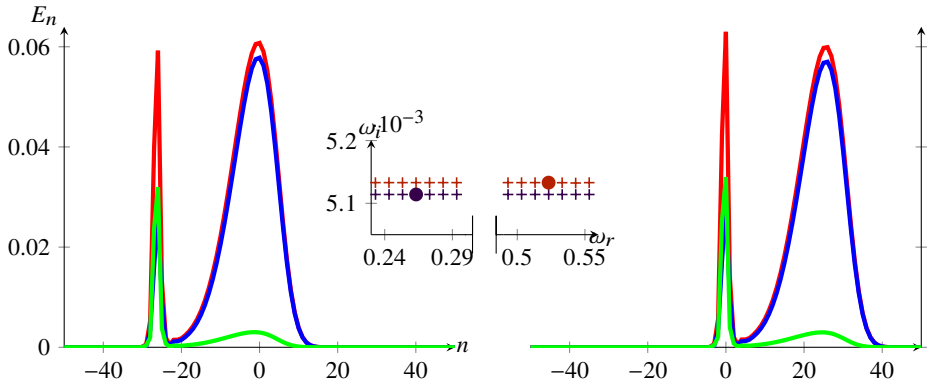

Figure 6: Energy per Floquet modes (red for total energy, blue for fluid kinetic energy, green for the wall potential and kinetic energy) at $\widetilde{Q} = 0.349$ (left) and $\widetilde{Q} = 0.350$ (right) with $V_R = 1$, Wo = 10, Re = 10000, $\alpha = 1$, $B_* = 4$ and $d_* = 0$. The frequency associated with the dominant peak is indicated by ●.

For the same set of parameters, the influence of $\widetilde{Q}$ on the stability of the system is shown in figure 7. For comparison purposes, the rigid case is also reported. We restrict our analysis to the sinuous symmetry. For the compliant wall case, the evolution of both temporal growth rates and circular frequencies are displayed for the first and second most amplified Floquet modes. The dominant Floquet frequency for each mode is selected using the methodology mentioned in the previous section. The TS mode distribution is seen to closely follow its rigid wall counterpart up to $\widetilde{Q} = 0.3$. When $\widetilde{Q}$ exceeds this value, however, its E_n-distribution exhibits two peaks and the mode consists of the superposition of TS and TWF waves (as illustrated in figure 6). For $\widetilde{Q}$ greater than 0.35 the energy peak is connected to the TWF wave. At this point, the dominant frequency for this mode is associated with wall dynamics as shown by the energy contributions in figure 6. For $\widetilde{Q}$ up to 0.5, we observe the co-existence of TWF and two-waves modes. For $0.5 < \widetilde{Q} < 0.6$, the two-waves modes is seen to be temporally damped. By contrast, the growth rate of TWF mode is increased for this range of $\widetilde{Q}$.

For larger values of $\widetilde{Q}$, the spectrum features a single unstable mode that shares the main characteristics of TWF modes.

In the next section, we will describe the spatio-temporal behaviour of Floquet eigenfunctions, for TWF, TS and two-waves modes.

6.4. *Spatial structure of eigenmodes*

The structure of TS and FSI Floquet modes are investigated in more detail by monitoring the wall-normal distribution of their flow kinetic energy. To that purpose we define the fluid kinetic energy of the Floquet mode (4.13–4.16) as

$$\hat{E}(y,t) = \frac{1}{2}\rho \left| \sum_n \hat{\mathbf{u}}^{(n)}(y) \exp\left(in\Omega t\right) \right|^2, \tag{6.2}$$

which is periodic in time and may be used to characterize the intracyclic dynamics, since it does not contain the long-term exponential growth (or decay) part.

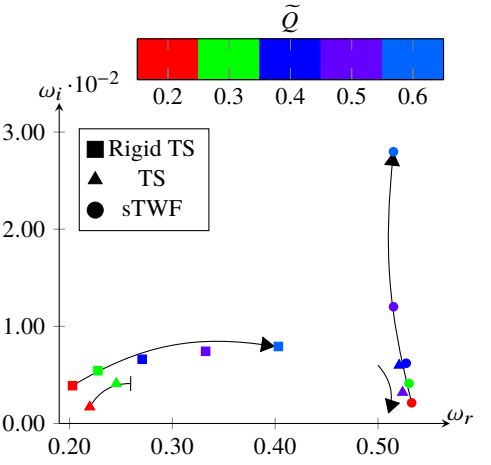

Figure 7: Spectra for different $\widetilde{Q}$ with $V_R = 1$, Wo = 10, Re = 10000, $\alpha = 1$, $B_* = 4$ and $d_* = 0$.

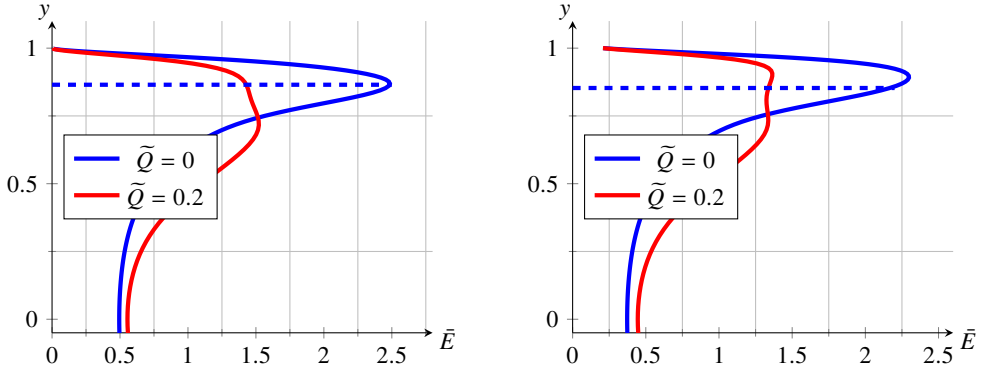

(a) Rigid channel.

(b) Compliant channel with $V_R = 1$.

Figure 8: The wall-normal distribution $\bar{E}(y)$ of averaged kinetic energy for the TS perturbations with $\widetilde{Q} = 0$, 0.2, Wo = 10, Re = 10000, $\alpha = 1$, $B_* = 4$ and $d_* = 0$. The critical layer position is indicated by blue dashed lines.

First, we will discuss the temporally averaged energy distribution, obtained as

$$\bar{E}(y) = \frac{1}{T}\int_0^T \hat{E}(t, y)\, dt. \tag{6.3}$$

In figure 8b, $\bar{E}(y)$ is shown for the TS mode for Wo = 10, $\widetilde{Q} = 0.2$, Re = 10000, $\alpha = 1$, $B_* = 4$, $d_* = 0$ and $V_R = 1$. For comparison purposes, the rigid wall and steady base flow cases are also reported in figure 8a.

We recall that for the case of a Poiseuille flow between flat rigid walls, $\bar{E}(y)$ should peak around the critical layer, i.e. the wall-normal position where the phase speed equals the base-flow velocity (Drazin & Reid 1981), as shown in figure 8a. For compliant walls and the steady flow case, a similar behaviour is observed (Davies & Carpenter 1997*a*), see figure 8b. However, a slight shift near the wall is observed for the peak in kinetic energy as a consequence of the stabilising effect of the compliant wall onto TS modes.

The distribution of $\bar{E}(y)$ for the time-periodic base flow exhibits a double peak structure

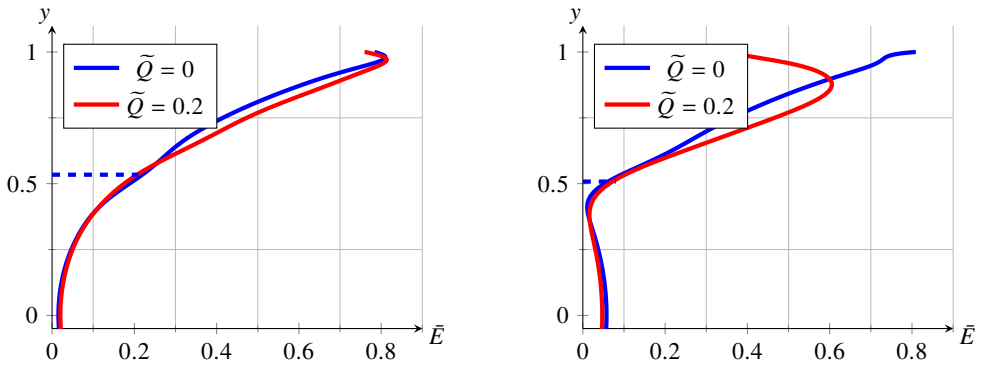

(a) Sinuous TWF mode. (b) Varicose TWF mode.

Figure 9: The wall-normal distribution of energy for TWF modes are shown for $\widetilde{Q} = 0$ and 0.2, $V_R = 1$, Wo = 10, Re = 10000, $\alpha = 1$, $B_* = 4$ and $d_* = 0$.

for both the rigid wall and compliant wall cases (see red curves in figure 8). This behaviour has also been observed by Singer *et al.* (1989) for the same flow case by using linearized direct numerical simulations and assuming rigid walls. They have shown that in a certain moment of the cycle, the mean flow profile exhibits an inflection point. These authors came to the conclusion that this second peak is a consequence of changes in the base flow profile during the cycle. Interestingly, figure 8 shows that the wall compliance enhances the first peak. More recently, Tsigklifis & Lucey (2017) also noticed this tendency for a similar case. The inner peak is also shifted closer to the wall due to wall compliance. It suggests that the stabilising effect of elastic walls onto TS modes still holds for pulsatile base flows.

The wall-normal distributions of $\bar{E}(y)$ for both varicose and sinuous TWF modes are shown in figure 9 for the same set of parameters. While for the sinuous symmetry, the TWF mode exhibits no significant changes in comparison with the steady flow case, the varicose TWF mode displays clearly a different structure near the walls. Indeed, the amplitude of vTWF mode peaks near $y = 0.9$ for the pulsatile base flow case, while it exhibits its maximum at the wall for the steady case. The consequences onto stability properties will be discussed in the next sections.

6.5. *Temporal dynamics of Floquet eigenmodes*

In this section, we investigate the intracyclic dynamics of the perturbations for the same configurations as in the previous section. For that purpose, we consider the instantaneous total perturbation energy, defined as

$$\tilde{E}(t) = \frac{1}{2h}\int_{-h}^{h} \hat{E}(y,t)\,dy + \tilde{E}_{WK}(t) + \tilde{E}_{WP}(t). \tag{6.4}$$

This quantity $\tilde{E}(t)$ is the sum of the instantaneous fluid kinetic energy and the kinetic and potential energies of the walls:

$$\tilde{E}_{WK}(t) = m\left|\sum_n \hat{\gamma}^{\pm(n)} \exp(in\Omega t)\right|^2, \tag{6.5}$$

$$\tilde{E}_{WP}(t) = (B\alpha^4 + T\alpha^2 + K)\left|\sum_n \hat{\eta}^{\pm(n)} \exp(in\Omega t)\right|^2. \tag{6.6}$$

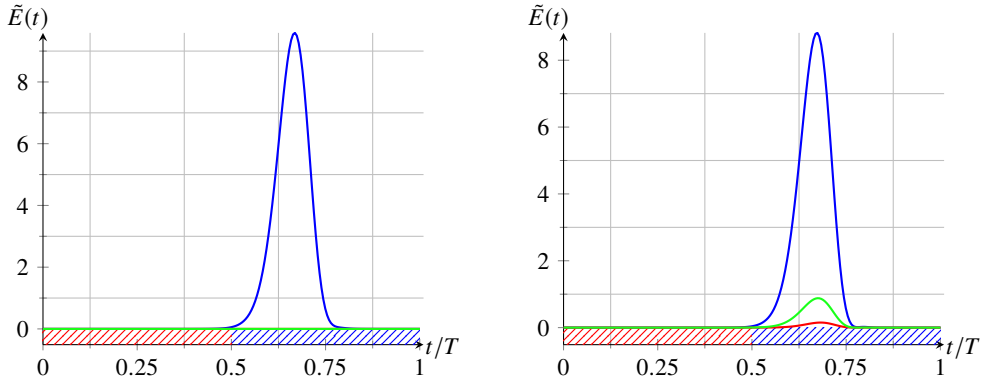

(a) Rigid channel. (b) Compliant channel.

Figure 10: The intracyclic modulation of energy for the TS perturbations with $\widetilde{Q} = 0.2$, Wo = 10, Re = 10000 and $\alpha = 1$. Color : blue for the fluid kinetic energy, green for the wall kinetic energy, red for wall potential energy. (a) Rigid channel, (b) compliant channel with $B_* = 4$, $d_* = 0$ and $V_R = 1$.

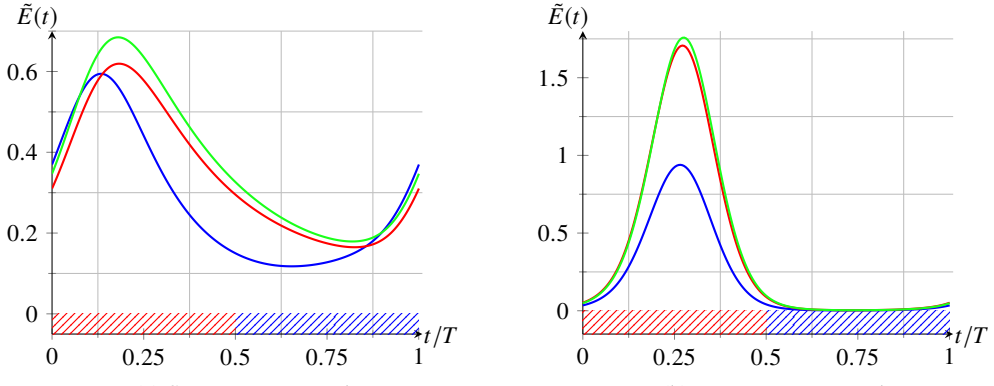

(a) Sinuous TWF mode. (b) Varicose TWF mode.

Figure 11: The intracyclic modulations of energy for the TWF perturbations with $\widetilde{Q} = 0.2$, $V_R = 1$, Wo = 10, Re = 10000, $\alpha = 1$, $B_* = 4$ and $d_* = 0$.

Recall that all these quantities are temporally periodic (with period Ω) since the complex exponential term $\exp(-i\omega t)$ has been removed.

We first consider the TS mode. Figure 10 shows the different contributions to $\tilde{E}(t)$ for Wo = 10, $\widetilde{Q} = 0.2$, Re = 10000, $B_* = 4$, $d_* = 0$ and $\alpha = 1$ for both the rigid case and compliant walls with $V_R = 1$. As noted by Pier & Schmid (2017) for the rigid case, the growth of $\tilde{E}(t)$ occurs in the deceleration phase of the base flow (indicated by regions hatched in red along the t-axis), while decay occurs during the acceleration phase (hatched in blue). This remains true for the compliant wall configuration (figure 10b). In particular, the dynamics of the perturbation is mainly driven by the flow kinetic energy while the wall energy is almost negligible. A similar behaviour has also been observed by Tsigklifis & Lucey (2017).

The intracyclic dynamics associated with TWF disturbances exhibits a markedly different behaviour as shown in figure 11. In contrast with the TS mode, the growth in total energy occurs during the acceleration phase of the base flow for both symmetries. Especially, walls

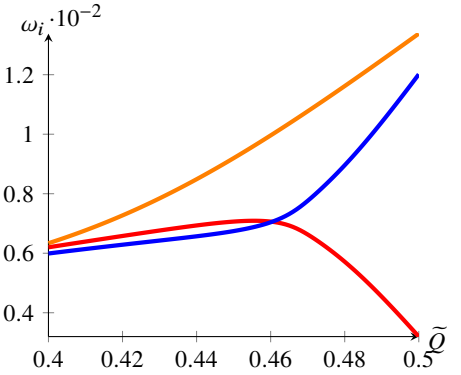

Figure 12: Dispersion relation with $V_R = 1$, Wo = 10, Re = 10000, $\alpha = 1$, $B_* = 4$ and $d_* = 0$ (blue for sTWF, red for TS and orange for sTWF at Re = 2000).

mainly contribute to the total energy growth whatever the symmetry that is considered. However, the fluid kinetic energy is less significant for the varicose case than the sinuous one.

6.6. *Interaction between TS and sTWF waves*

As mentioned earlier, a two-waves mode (i.e. where both FSI and TS waves interact) may emerge for a given of set of parameters.

Here we will further investigate the occurence of this Floquet mode. To that purpose, the parameters Wo = 10, $B_* = 4$, $d_* = 0$, $V_R = 1$ and $\alpha = 1$ are considered. Two Reynolds numbers will be studied Re = 2000 and Re = 10000 (i.e. corresponding to either subcritical or supercritical regime with respect to TS mode associated with the rigid case.)

In figure 12, the variation with $\widetilde{Q}$ of the temporal growth rates for both two-waves mode and sTWF mode are shown. For Re = 10000, the figure shows that these modes merge at $\widetilde{Q} \approx 0.46$. Beyond this value, we observe that both modes diverge away from one other. Then, one mode exhibits a strong increase in temporal growth rate. This behaviour is similar to modes coalescence found in the steady case between TS and sTWF modes when increasing wall dissipation, giving rise to the so-called transition mode. Interestingly, for pulsatile flow, this phenomenon also appears for $d_* = 0$. Then, for $\widetilde{Q} \approx 0.46$, we can associate this mode to a transition mode. For comparison purpose, the case for Re = 2000 is also reported in figure 12. The merging is not observed here because TS wave is temporally damped for this Reynolds number.

To better illustrate the temporal dynamics associated with the two-waves mode and transition mode, we show in figure 13 the intracyclic evolution of the total perturbation energy $\tilde{E}(t)$ for different pulsation amplitudes $\widetilde{Q}$ and the sinuous symmetry. On one hand, the TWF mode exhibits almost no effect as $\widetilde{Q}$ is increased in the range 0.38–0.48 for both Reynolds numbers. On the other hand, the two-waves mode presents an interesting intracylic dynamics.

At $\widetilde{Q} = 0.38$, growth occurs for both the acceleration and deceleration phases of the base flow. It is consistent with the fact that this Floquet mode shares common features with both TS and TWF waves. When increasing $\widetilde{Q}$, the growth associated with the acceleration phase is increasing. On the contrary, figure 13 shows that the energy peak in the deceleration phase is damped with $\widetilde{Q}$. It means that the two-waves mode is mainly driven by its TWF contribution as $\widetilde{Q}$ is increased from 0.38 to 0.48. In particuler, beyond $\widetilde{Q} = 0.46$, the TS wave

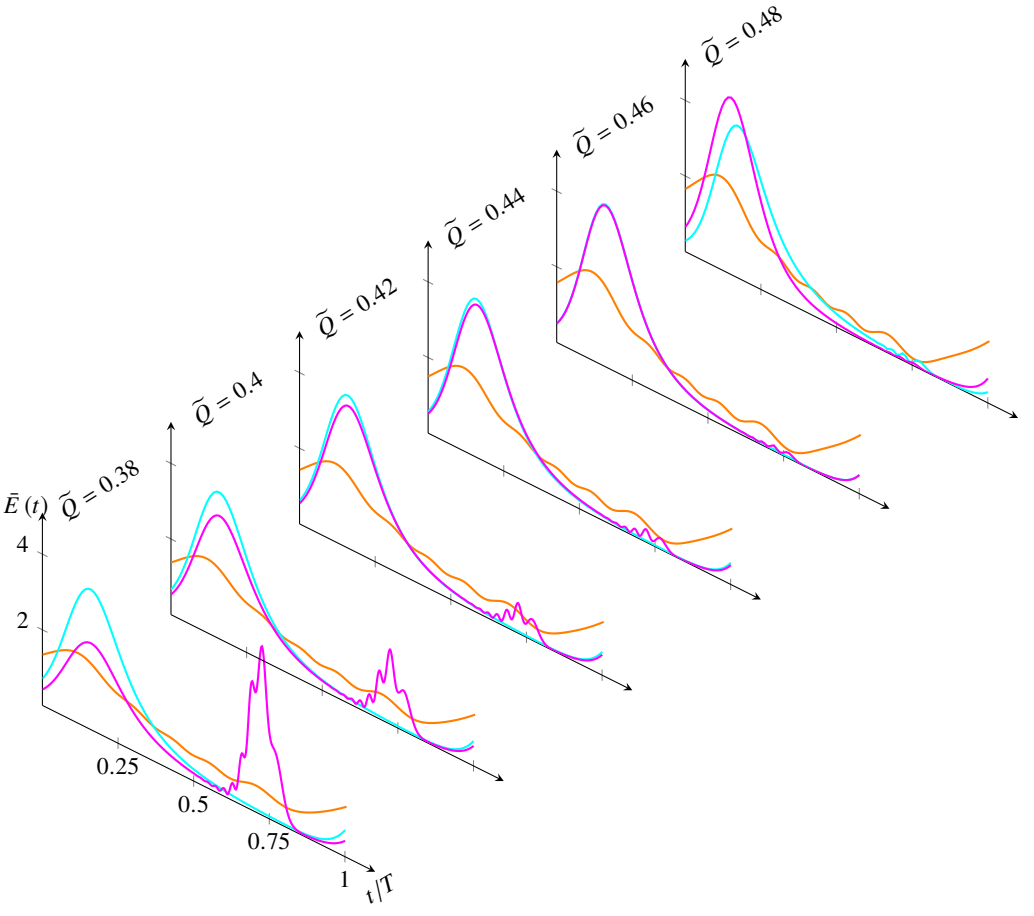

Figure 13: Intracyclic evolution of the total perturbation energy $\tilde{E}(t)$ with $V_R = 1$, Wo = 10, Re = 10000, $\alpha = 1$, $B_* = 4$ and $d_* = 0$ (Cyan for sTWF, Fuchsia for TS and orange for sTWF at Re = 2000).

contribution is negligible. As a consequence, at $\widetilde{Q} = 0.46$, the variation of $\tilde{E}(t)$ for TWF and two-waves modes are almost undistinguishable. This corresponds to the coalescence observed in figure 12. Beyond $\widetilde{Q} = 0.46$, this transition mode shows the same characteristics as the TWF instabilities, namely, a growth of energy in the acceleration phase of the base flow.

The intracyclic behaviour associated with the two-waves mode displays a low-frequency beating during the deceleration phase of the base flow for $0.38 \leqslant \widetilde{Q} \leqslant 0.46$ (see figure 13). This phenomenon results from an interference between two waves of slightly different frequencies. Especially, for this range of $\widetilde{Q}$, TS and sTWF modes merge to form a wavepacket whose frequency is the difference of the two frequency peaks. The Fourier density distribution of the two-waves mode for $\widetilde{Q} = 0.38$ is shown in figure 14a. The difference between the two peaks indeed corresponds exactly to the frequency beating observed in figure 14b.

To further illustrate this point, $\tilde{E}(t)$ has been computed by filtering the Fourier components in the neighbourhood of either the TS wave or the sTWF wave, using components from the ranges hatched respectively in fuchsia or orange in figure 14a. The plots of figure 14b show

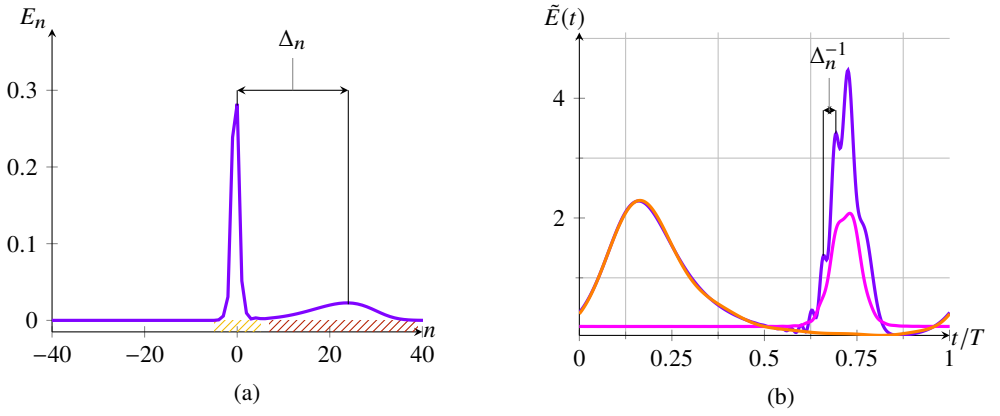

Figure 14: (a) Fourier density distribution and (b) filtered intracyclic total energy for the two-waves mode with $\widetilde{Q} = 0.38$, $V_R = 1$, Wo = 10, Re = 10000, $\alpha = 1$, $B_* = 4$ and $d_* = 0$. Blue: full dynamics, fuchsia: TS wave dynamics and orange: sTWF wave dynamics.

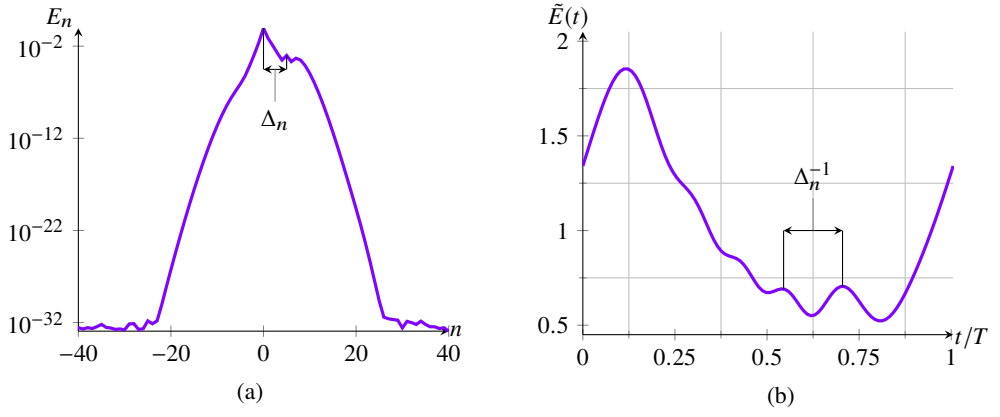

Figure 15: (a) Fourier density distribution and (b) intracyclic energy variation for the sTWF mode with $\widetilde{Q} = 0.38$, $V_R = 1$, Wo = 10, Re = 2000, $\alpha = 1$, $B_* = 4$ and $d_* = 0$.

that intracyclic dynamics pertaining to either the TS wave or the sTWF wave is recovered and the beating phenomenon is then suppressed.

To conclude this section, we show in figure 15 the case of the sinuous TWF mode at Re = 2000. As noted earlier, at this subcritical Reynolds number, the TS wave is damped. Therefore, the interference appears only as small amplitude oscillations (see figure 15b). The harmonics of the two waves are hard to distinguish in figure 15a, which results in a greater period for the secondary oscillations.

6.7. *Neutral curves*

The purpose of this section is to identify the critical parameters for the onset of instabilities over a wide parameter space. To this end, we first compute the neutral boundaries (i.e. corresponding to $\omega_i = 0$). For the rigid case, the neutral stability curves are commonly presented in the (Re, α) plane within a temporal framework. However, it has been shown by Lebbal *et al.* (2022) that the Reynolds number has only a weak effect onto the TWF instability modes for a steady base flow. Hence, neutral stability curves associated with TWF Floquet modes will be displayed in the (V_R, α)-plane hereafter.

Figure 16 shows neutral boundaries associated with the TS Floquet mode for $\widetilde{Q} = 0$, 0.1 and 0.2, Wo = 10, 12, 14 and $V_R = 0.2$, 0.4, 0.6 and 0.8. One may recall that for the rigid case the oscillating component reduces instability for Wo > 13, while it has a destabilising effect at lower frequencies (Pier & Schmid 2017). The effect of wall compliance is therefore here investigated in a neighbourhood of Wo = 13.

Increasing the wall compliance (i.e. increasing V_R) leads to a reduction of the range of unstable streamwise wave numbers and an increase of the critical Reynolds numbers for all flow parameters. Similar behaviour is also observed for the steady base flow (Lebbal *et al.* 2022). In addition, the stabilising effect of $\widetilde{Q}$ onto TS Floquet modes for Wo > 13 is also recovered for the compliant walls case. Finally, for moderate pulsation amplitudes $\widetilde{Q}$, the stabilisation mechanism caused by wall flexibility seems not to be affected by the base flow modulation.

For Wo = 20, neutral boundaries in the (V_R, α)-plane for the TWF Floquet modes are shown in figure 17 for both symmetries. On one hand, the upper bound of the unstable wave number range grows lineary with the amplitude of the pulsation. On the other hand, the lower bound is almost unchanged by the pulsatile base flow components.

Near the critical reduced velocity, referenced as V_R^c hereafter (i.e. the value of V_R that corresponds to the onset of instability), the varicose TWF is weakly stabilised for $\widetilde{Q} < 0.4$. For larger values of $\widetilde{Q}$, a destabilisation effect is observed. For the sinuous symmetry, a decrease in V_R^c is observed when the amplitude of the base flow modulation is increased, for all values of $\widetilde{Q}$ that are considered.

Neutral stability curves are also displayed in figure 18 for the same parameters except that Wo is fixed to 10. Comparison of figures 17 and 18 shows that the Womersley number has a weak effect onto the neutral boundaries for these TWF Floquet modes.

6.8. *Influence of* $\widetilde{Q}$ *and* Wo *onto temporal growth rates*

In this section, we investigate the combined effect of wall flexibility and pulsatile base flow parameters ($\widetilde{Q}$ and Wo) onto the temporal growth rates of TWF and TS Floquet modes. Results are conveniently summarized by monitoring the growth rate $\omega_i^{\max}$ associated with the most unstable streamwise instability (i.e. $\omega_i^{\max} = \max_\alpha \omega_i$) for a given set of fluid and wall parameters. For illustration purposes, $B_* = 4$ and $d_* = 0$ are fixed.

Figures 19a and 19b show the variation of the maximum temporal growth rates with $\widetilde{Q}$ and Wo of the TS mode for both the rigid case in (a) and compliant walls ($V_R = 0.2$) in (b).

The TS Floquet modes exhibit similar dynamics whatever the case considered (either rigid or compliant walls). For Wo $\geqslant$ 14, the temporal growth rate decays with $\widetilde{Q}$ for both rigid and flexible cases while it increases for Wo $\leqslant$ 13. One may recall that a similar behaviour is observed for the rigid case (Pier & Schmid 2017).

Figure 20 illustrates the effect of Wo and $\widetilde{Q}$ onto travelling-wave flutter Floquet modes for $V_R = 1$. The temporal growth rate for the varicose vTWF mode presents two distinguishable phases (figure 20a). For small and moderate values of $\widetilde{Q}$, $\omega_i^{\max}$ is damped. Then, one may observe a growth of $\omega_i^{\max}$ as $\widetilde{Q}$ is increasing. The turning point depends on the Womersley number. Especially, the corresponding $\widetilde{Q}$ is seen to increase with Wo.

The distribution of $\omega_i^{\max}$ for the sinuous symmetry exhibits a different behaviour. For weakly pulsatile base flows ($\widetilde{Q} < 0.2$), the sTWF mode is destabilised whatever the Wo number that is considered. In particular, this instability is strongly enhanced for the small frequencies of modulation Wo. For moderate values of $\widetilde{Q}$ ($0.2 < \widetilde{Q} < 0.5$), a more complex behaviour is observed. For this range of amplitudes, the sTWF mode interacts with TS

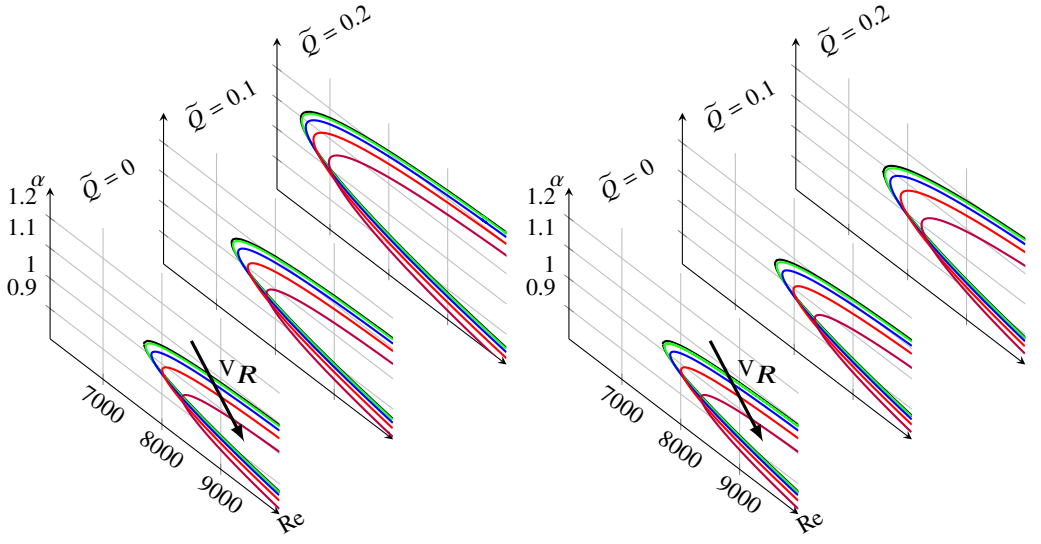

(a) Wo = 10.

(b) Wo = 12.

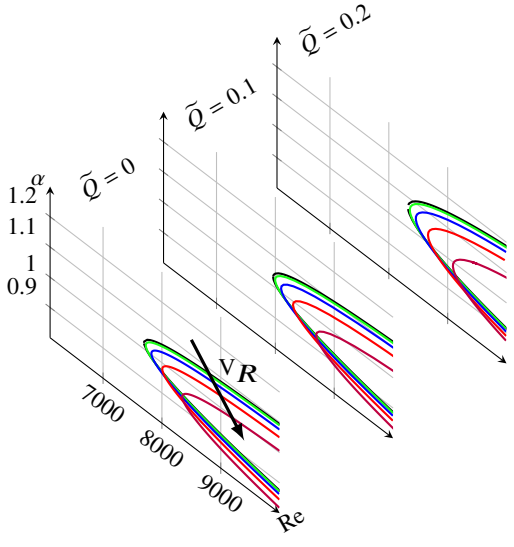

(c) Wo = 13.

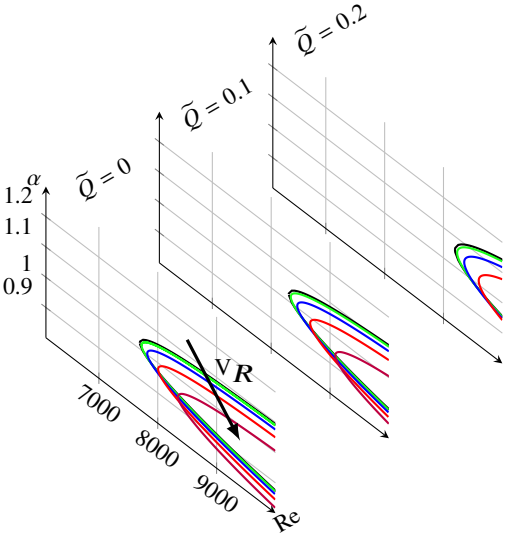

(d) Wo = 14.

Figure 16: Neutral curves in the (α, Re)-plane for TS mode with $B_* = 4$ and $d_* = 0$ for different amplitudes $\widetilde{Q} = 0, 0.1, 0.2$ and frequencies Wo = 10, 12, 13, 14, with V_R varying from 0. to 0.8. The associated colors are respectively black, green, blue, red and brown.

Floquet mode, and we can no longer distinguish between these two waves. Beyond this point, $\omega_i^{\max}$ strongly increases and reaches similar values as its varicose counterpart.

An intracyclic modulation amplitude $E_{\min}^{\max}$, defined as the ratio of the maximum to the minimum of $\tilde{E}(t)$, is computed for the same parameter range as in figure 20, for travelling-

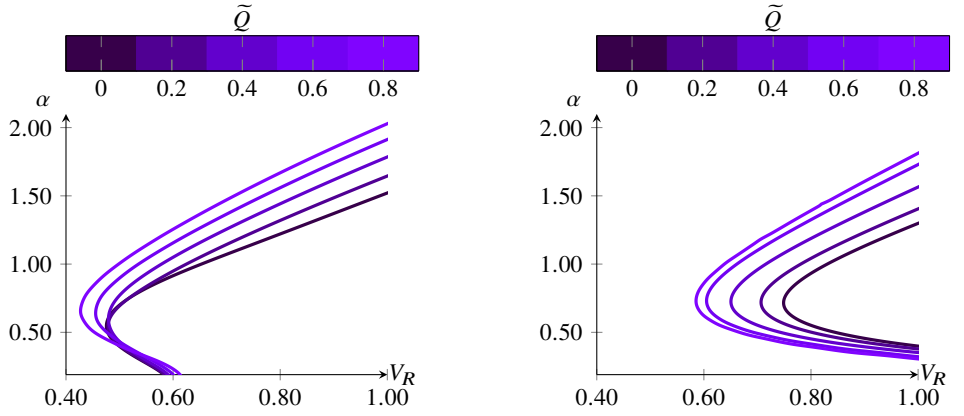

(a) vTWF mode. (b) sTWF mode.

Figure 17: Neutral curves in the (α, V_R)-plane for TWF modes with Wo = 20, Re = 10000, $B_* = 4$ and $d_* = 0$.

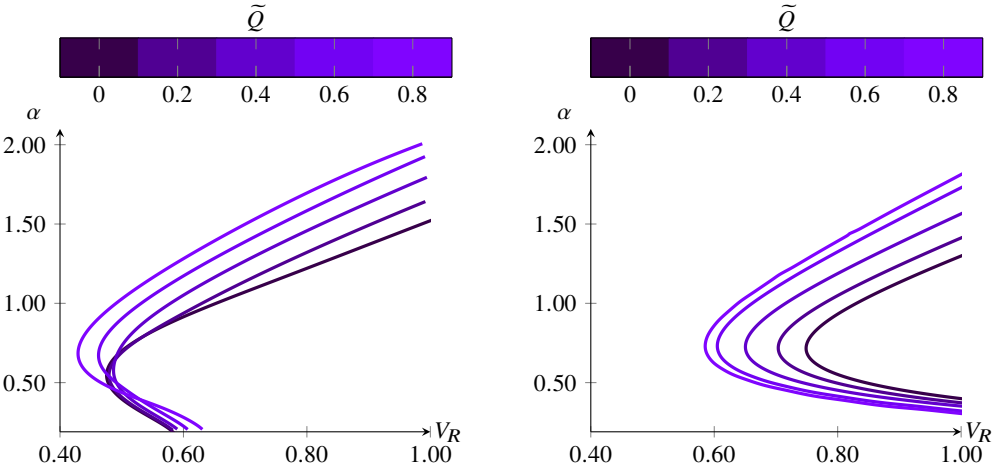

(a) vTWF mode. (b) sTWF mode.

Figure 18: Neutral curve in the (α, V_R)-plane for TWF modes with Wo = 10, Re = 10000, $B_* = 4$ and $d_* = 0$.

wave flutter Floquet modes only. For the varicose symmetry, the plots in figure 21a show that $E_{\text{min}}^{\text{max}}$ increases for all Wo under consideration. The evolution of $E_{\text{min}}^{\text{max}}$ for the sinuous symmetry is displayed in figure 21b. The figure shows that the sinuous TWF Floquet modes exhibit smaller amplitude variations than their varicose counterparts. In addition, for $\widetilde{Q} > 0.5$, a saturation of $E_{\text{min}}^{\text{max}}$ is observed. Such a behaviour occurs beyond the collapse of TWF and TS Floquet modes. One may thus suggest that it is a consequence of the emergence of a transition mode. Comparison with figure 11 also reveals that the very large values of $E_{\text{min}}^{\text{max}}$ observed for the vTWF modes (figure 21a) are mainly due to the fact that $\tilde{E}(t)$ drops to extremely low levels during the accelation phase of the pulsating cycle (figure 11b).

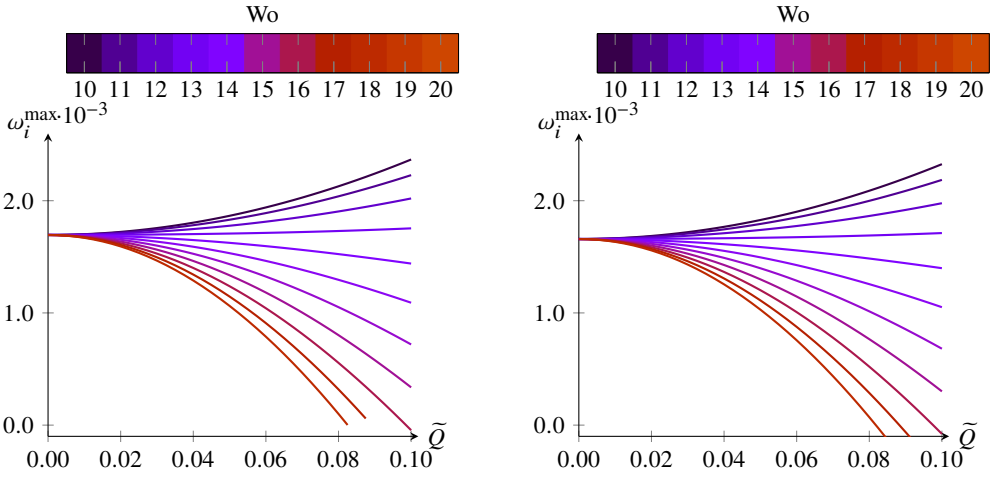

(a) Rigid wall. (b) V_R =0.2.

Figure 19: TS Floquet mode. Maximum temporal growth rates $\omega_i^{\max}$ for different amplitudes $\widetilde{Q} = 0, \ldots, 0.1$ and frequencies Wo = 10, . . . , 20, with Re = 10000, $B_* = 4$ and $d_* = 0$.

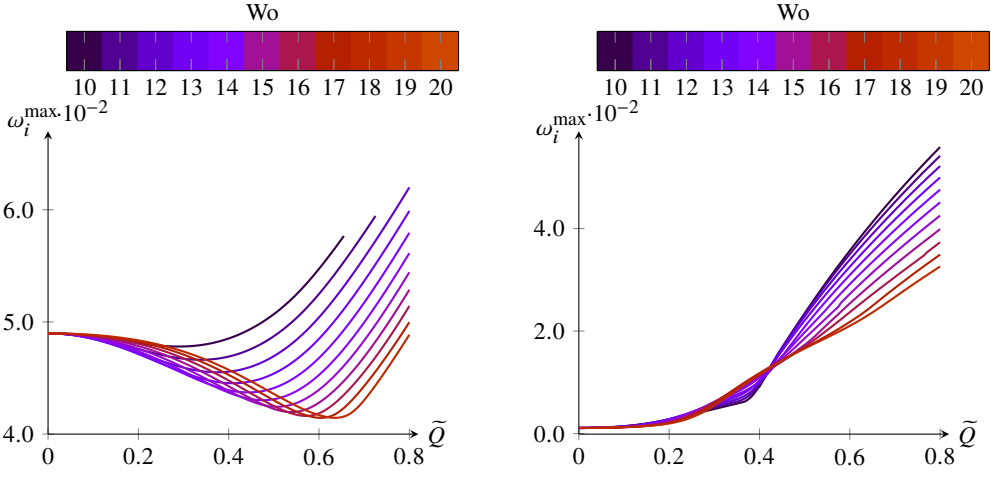

(a) vTWF $V_R = 1$. (b) sTWF $V_R = 1$.

Figure 20: Maximal temporal growth rates $\omega_i^{\max}$ for different amplitudes $\widetilde{Q} = 0, \ldots, 0.7$ and frequencies Wo = 10, . . . , 20, with Re = 10000, $B_* = 4$ and $d_* = 0$.

6.9. *Critical parameters for onset of instability*

A complete two-dimensional instability analysis is now performed by exploring a wide range of wall and flow parameters. In a effort to summarize the different results only critical Reynolds numbers (Re^c) and critical reduced velocities (V_R^c) are monitored (corresponding to the onset of TS or TWF Floquet modes, respectively).

The variations of Re^c for the TS mode are computed for $V_R = 0.2$ and $V_R = 0.6$ for different pulsatile flow parameters in figure 22. Beyond Wo = 13, the TS Floquet modes are stabilised by the pulsatile flow component. For lower frequencies, the opposite behaviour is observed. For example, at Wo = 20, the critical Reynolds number for $\widetilde{Q} = 0.10$ is already about 50%

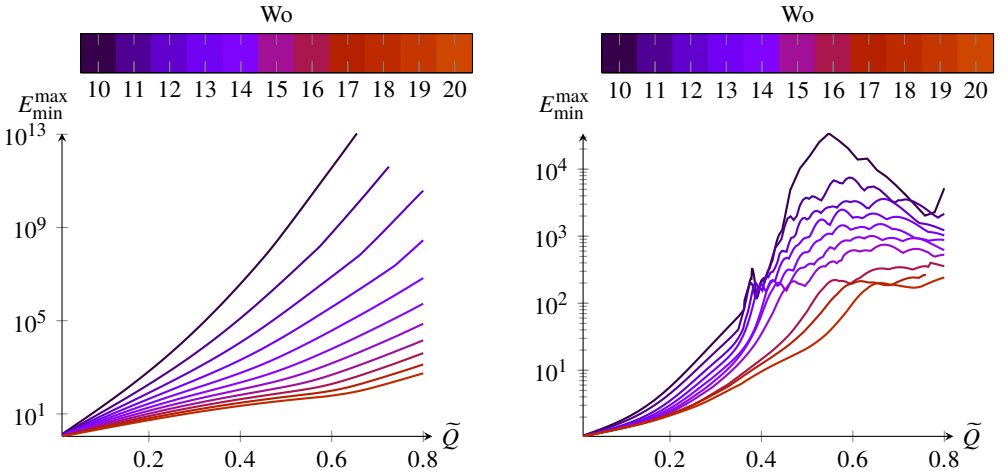

(a) vTWF modes. (b) sTWF modes.

Figure 21: The amplitude of the modulation ratio $E_{\min}^{\max}$ for different amplitudes $\widetilde{Q} = 0$, ..., 0.7 and frequencies Wo = 10, ..., 20, with Re = 10000, $B_* = 4$, $d_* = 0$ and $\mathrm{V}_R = 1$.

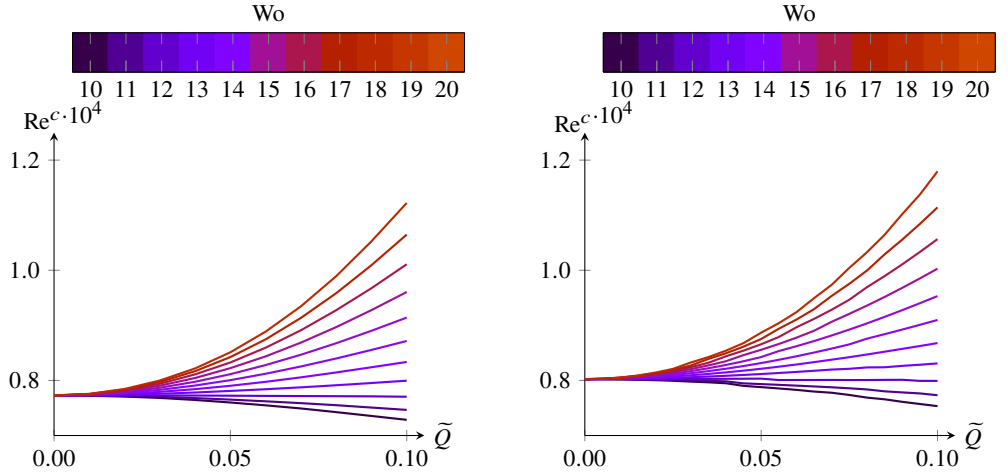

(a) $\mathrm{V}_R = 0.2$. (b) V_R =0.6.

Figure 22: Critical Reynolds number Re^c for TS mode with $B_* = 4$ and $d_* = 0$.

larger than the value found for the Poiseuille flow case ($\widetilde{Q} = 0$). The dynamics including compliant walls is thus found to be very similar to the rigid walls case (see Pier & Schmid (2017)).

The critical reduced velocity V_R^c for the TWF modes are shown in figure 23. The varicose travelling-wave flutter displays two phases. For moderate pulsation amplitudes ($\widetilde{Q} < 0.4$), the instability is weakly stabilised. For higher pulsation amplitudes, the vTWF mode is destabilised for all the frequencies studied. Unlike the vTWF, the sinuous TWF mode shows a monotonic destabilisation as the pulsation amplitude is increased. The Womersley numbers considered here have almost no effect on the critical curves. Note that even for highly pulsatile flows, onset of TWF instability is always due to the varicose symmetry.

In order to systematically study the linear stability over the entire parameter space, the

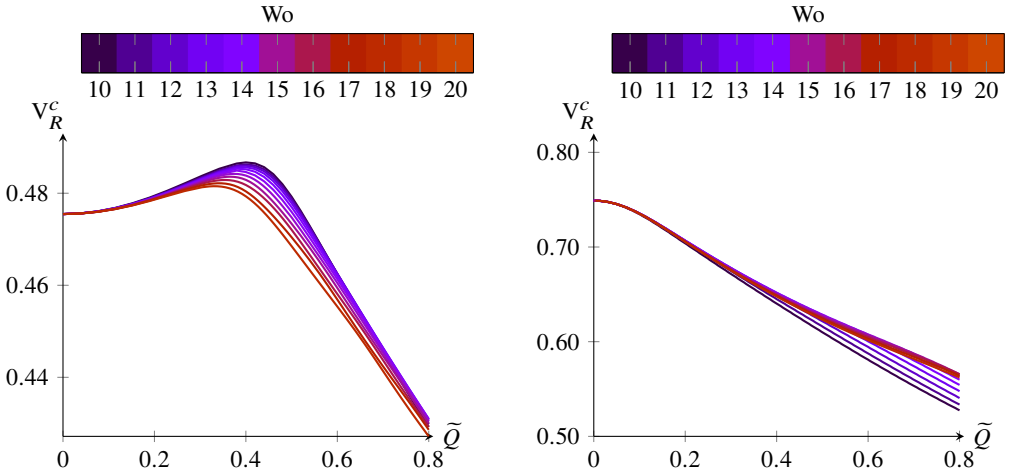

(a) Varicose TWF. (b) Sinuous TWF.

Figure 23: Critical reduced velocities V_R^c for TWF modes and different Wo numbers. The other parameters are: Re = 10000, $B_* = 4$ and $d_* = 0$.

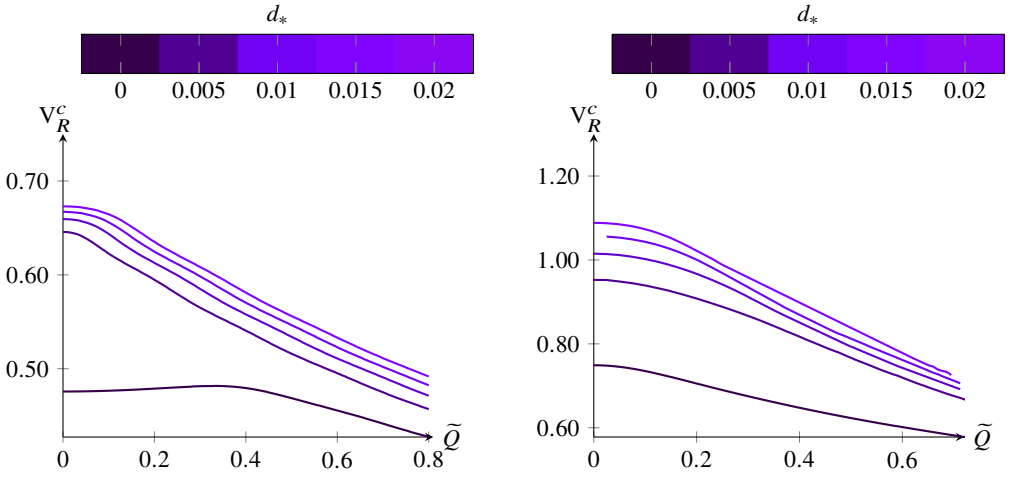

(a) Varicose TWF. (b) Sinuous TWF.

Figure 24: Critical reduced velocities V_R^c for TWF modes for different d_*. The other parameters are: Wo = 20, Re = 10000 and $B_* = 4$.

critical reduced velocity V_R^c is also computed for various wall dissipations d_* (figure 24), flexural rigidities B_* (figure 25) and Reynolds numbers Re (figure 26).

According to the energy classification of Benjamin (1963) and Landahl (1962), the dissipation has a stabilising effect on the travelling-wave flutter instabilities. The plots in figure 24 show the variation of the critical reduced velocity with wall dissipation d_*. For a Poiseuille base flow ($\widetilde{Q} = 0$), the critical V_R^c is almost multiplied by a factor 2 when d_* is varied from 0 to 0.02.

An increase in $\widetilde{Q}$ leads to stabilise the flow for all values of d_* that have been considered (see figure 24). In particular, the overall behaviour is quite similar for d_* varying from 0.005 to 0.04. The critical V_R^c is nearly constant for $\widetilde{Q}$ up to 0.05. Beyond this value, V_R^c decreases

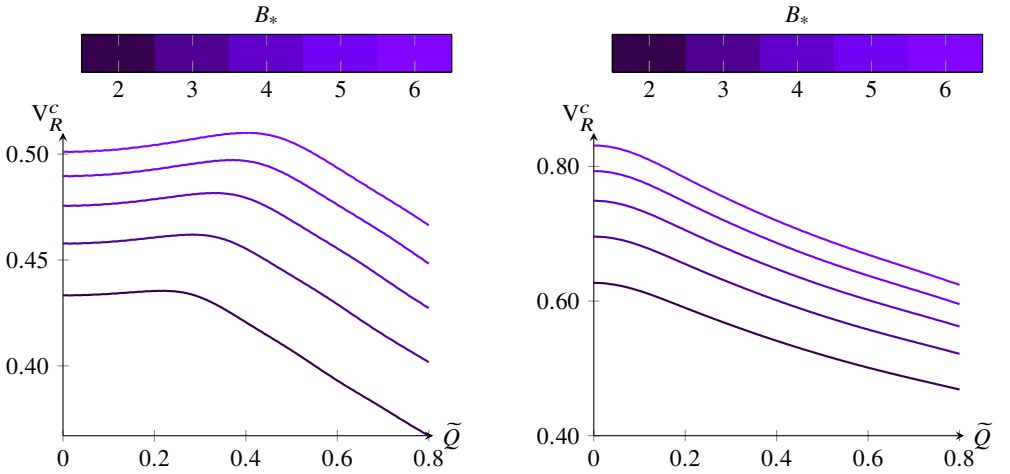

(a) Varicose TWF. (b) Sinuous TWF.

Figure 25: Critical V_R^c for TWF modes for different B_*. The other parameters are: Wo = 20, Re = 10000 and $d_* = 0$.

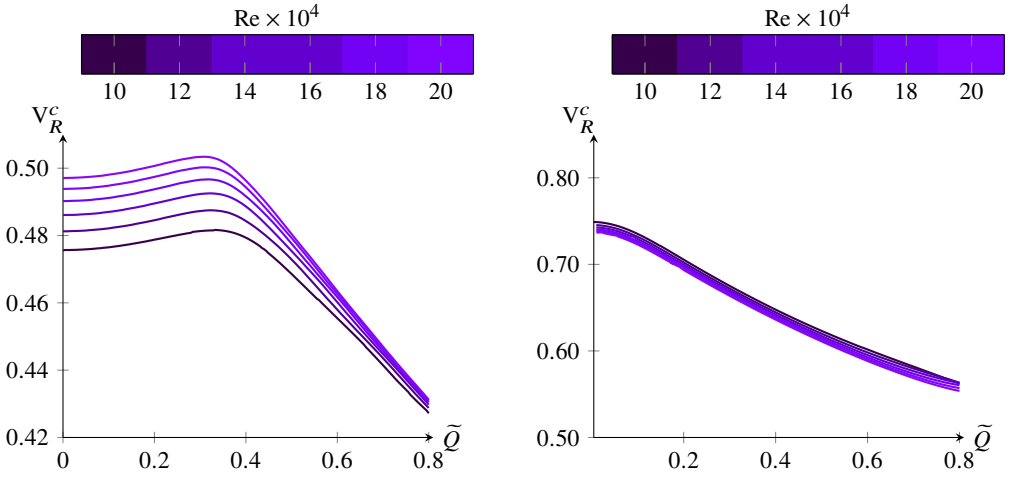

(a) Varicose TWF. (b) Sinuous TWF.

Figure 26: Critical V_R^c for TWF modes for different Re numbers. The other parameters are: Wo = 20, $B_* = 4$ and $d_* = 0$.

almost linearly with $\widetilde{Q}$ at a similar rate of change. Interestingly, the symmetry of the Floquet mode appears to have a negligible effect onto V_R^c for this range of parameters.

The effect of flexural rigidity is illustrated in figure 25. Increasing B_* results in stabilising the TWF Floquet modes for all $\widetilde{Q}$ that are considered. However, the overall shape of these curves is almost unaffected by B_* for both sinuous and varicose cases. For the varicose case, a nearly constant value of V_R^c is observed up to $\widetilde{Q} = 0.3$. Beyond $\widetilde{Q} = 0.4$, the critical V_R^c is seen to decrease almost linearly with $\widetilde{Q}$ for all flexural rigidities that have been investigated. In particular, the slope seems to be independent of B_*.

The sinuous case appears to be more stable than its varicose counterpart. As for the varicose

symmetry, the overall tendency is not affected by B_*. A slight decrease in V_R^c is observed for $\widetilde{Q}$ up to 0.1. Beyond $\widetilde{Q} = 0.4$, V_R^c exhibits an almost linear behaviour with $\widetilde{Q}$.

Finally, the influence of the Reynolds number onto V_R^c is shown in figure 26. The onset of Floquet TWF modes are almost unchanged by the Reynolds number for both the varicose and sinuous TWF modes. The insensitivity to Re is more pronounced when $\widetilde{Q}$ is increased to large amplitudes. This weak influence has already been reported for the steady case (Lebbal *et al.* 2022).

7. Conclusions

In this paper, we have systematically investigated the rich dynamics resulting from perturbations developing in harmonically pulsating flows between two compliant walls. The stability analysis is restricted to the time-asymptotic behaviour of the flow perturbation and to the two-dimensional case within the framework of Floquet theory. A numerical solution strategy has been implemented that is free of spurious modes and greatly reduces the computational effort.

When accounting for wall compliance, we show that the most relevant control parameter is the reduced velocity V_R for travelling-wave flutter Floquet modes. Especially, the Reynolds number appears to have a negligible influence on these modes. As already observed for the steady case (Lebbal *et al.* 2022), the most unstable modes are associated with the varicose symmetry. For the pulsatile flow configurations, we show that the instability onset for these modes is mainly driven by the amplitude of the pulsation rather than its frequency. For $\widetilde{Q}$ in the range 0–0.4 and varicose perturbations, the pulsatile base flow is seen to weakly stabilise the TWF Floquet modes (*i.e.* the critical reduced velocity increases) with respect to the steady flow case. The opposite behaviour is observed for $\widetilde{Q}$ larger than 0.4. For the sinuous symmetry, we always observe a flow destabilisation with an increase of $\widetilde{Q}$. When accounting for the wall dissipation, we show that an increase of d_* tends to stabilise the travelling-wave flutter Floquet modes for both symmetries whatever the value of $\widetilde{Q}$ in agreement with Benjamin's classification (Benjamin 1963). For the Tollmien–Schlichting Floquet modes, the intracyclic dynamics exhibits strong similarities with the pulsatile flow case in a rigid channel (Pier & Schmid 2017). However, a stronger stabilisation is observed when wall flexibility comes into play.

On one hand, it has been shown that Benjamin's classification still holds for a wide range of parameters. Especially, for fluid-structure interaction modes, similar general trends are observed for steady and pulsatile flow configurations. But on the other hand, this study has also revealed a more complex flow dynamics that is not found when wall flexibility or pulsating base flow are studied independently. In particular, a new type of transition mode has been discovered that emerges due to the coalescence of two Floquet modes, even in the absence of wall dissipation. The first Floquet mode combines properties of both Tollmien–Schlichting modes and travelling-wave flutter modes. This coupling leads to interference that generates a low-frequency beating during the intracyclic dynamics. The second Floquet mode shares the main properties of a travelling-wave flutter mode. When increasing the pulsation amplitude, these two modes merge into a more unstable Floquet mode.

Extension of the present study to nonmodal stability analyses can be considered in a future work, continuing the investigations of Tsigklifis & Lucey (2017) and Pier & Schmid (2021). Finally, it would also be interesting to generalise our analyses to pipe geometries which cover more biologically significant phenomena. The theoretical developments and numerical tools that have been used in the present investigation can be easily adapted to a formulation in cylindrical coordinates, following the same approach used by Pier & Schmid (2021).

Acknowledgements.
Fédération lyonnaise de modélisation et sciences numériques (FLMSN) is greatfully acknowledged for providing access to high-performance computing resources.

Declaration of interests.
The authors report no conflict of interest.

Author ORCIDs.
Smail Lebbal, https://orcid.org/0000-0003-4054-6094;
Frédéric Alizard, https://orcid.org/0000-0002-1741-1602;
Benoît Pier, https://orcid.org/0000-0001-8663-8694.

REFERENCES

Benjamin, T. B. 1959 Shearing flow over a wavy boundary. *J. Fluid Mech.* **6**, 161–205.

Benjamin, T. B. 1960 Effects of a flexible boundary on hydrodynamics stability. *J. Fluid Mech.* **9**, 513–532.

Benjamin, T. B. 1963 The threefold classification of unstable disturbances in flexible surfaces bounding inviscid flows. *J. Fluid Mech.* **16**, 436–450.

Blennerhassett, P. J. & Bassom, A. P. 2006 The linear stability of high-frequency oscillatory flow in a channel. *J. Fluid Mech.* **556**, 1–25.

Boyd, J. P. 2001 *Chebyshev and Fourier Spectral Methods*. New York: Dover.

Carpenter, P. W. & Garrad, A. D. 1985 The hydrodynamic stability of flow over Kramer-type compliant surfaces. Part 1. Tollmien–Schlichting instabilities. *J. Fluid Mech.* **155**, 465–510.

Carpenter, P. W. & Garrad, A. D. 1986 The hydrodynamic stability of flow over Kramer-type compliant surfaces. Part 2. Flow-induced surface instabilities. *J. Fluid Mech.* **170**, 199–232.

Chiu, J.-J. & Chien, S. 2011 Effects of disturbed flow on vascular endothelium: pathophysiological basis and clinical perspectives. *Physiol. Rev.* **91**, 327–387.

Davies, C. & Carpenter, P. W. 1997*a* Instabilities in a plane channel flow between compliant walls. *J. Fluid Mech.* **352**, 205–243.

Davies, C. & Carpenter, P. W. 1997*b* Numerical simulation of the evolution of Tollmien–Schlichting waves over finite compliant panels. *J. Fluid Mech.* **335**, 361–392.

Davis, S. H. 1976 The stability of time-periodic flows. *Annu. Rev. Fluid Mech.* **8**, 57–74.

Drazin, P. G. & Reid, W. H. 1981 *Hydrodynamic Stability*. Cambridge: Cambridge University Press.

Gad-el-Hak, M. 1986 Boundary layer interactions with compliant coatings: An overview. *Appl. Mech. Rev.* **39**, 511–524.

Gad-el-Hak, M. 1996 Compliant coatings: A decade of progress. *Appl. Mech. Rev.* **49**, S147–S157.

Gaster, M. 1988 Is the dolphin a red herring? In *IUTAM Symposium on Turbulence Management and Relaminarisation* (ed. H. W. Liepmann & R. Narasimha), pp. 285–304. Springer.

Gray, J. 1936 Studies in animal locomotion: VI. The propulsive powers of the dolphin. *J. Exp. Biol.* **13**, 192–199.

von Kerczek, C. H. 1982 The instability of oscillatory plane Poiseuille flow. *J. Fluid Mech.* **116**, 91–114.

Kramer, M. 1957 Boundary layer stabilization by distributed damping. *J. Aeronaut. Sci.* **24**, 459–505.

Ku, D. N. 1997 Blood flow in arteries. *Annu. Rev. Fluid Mech.* **29**, 399–434.

Kumaran, V. 2021 Stability and the transition to turbulence in the flow through conduits wih compliant walls. *J. Fluid Mech.* **924**, P1.

Landahl, M. T. 1962 On the stability of laminar boundary-layer flow over a flat plate with a compliant surface. *J. Fluid Mech.* **13**, 609–632.

de Langre, E. 2000 Analyse dimensionnelle en interaction fluide–structure. *La Houille Blanche* **3/4**, 14–18.

Lebbal, S., Alizard, F. & Pier, B. 2022 Revisiting the linear instabilities of plane channel flow between compliant walls. https://hal.archives-ouvertes.fr/hal-03337441, accepted for publication in *Phys. Rev. Fluids*.

Manning, M. L., Bamieh, B. & Carlson, J. M. 2007 Descriptor approach for eliminating spurious eigenvalues in hydrodynamic equations. https://arxiv.org/abs/0705.1542.

Miles, J. W. 1957 On the generation of surface waves by shear flows. *J. Fluid Mech.* **3**, 185–199.

800 O'Rourke, M. F. & Hashimoto, J. 2007 Mechanical factors in arterial aging: A clinical perspective. *Journal*
801 *of the American College of Cardiology* **50**, 1–13.
802 Peyret, R. 2002 *Spectral Methods for Incompressible Viscous Flow*. New York: Springer.
803 Pier, B. & Schmid, P. J. 2017 Linear and nonlinear dynamics of pulsatile channel flow. *J. Fluid Mech.* **815**,
804 435–480.
805 Pier, B. & Schmid, P. J. 2021 Optimal energy growth in pulsatile channel and pipe flows. *J. Fluid Mech.*
806 **926**, A11.
807 Schumack, M. R., Schultz, W. & Boyd, J. P. 1991 Spectral method solution of the Stokes equations on
808 nonstaggered grids. *J. Comput. Phys.* **94**, 30–58.
809 Sen, P. K. & Arora, D. S. 1988 On the stability of laminar boundary-layer flow over a flat plate with a
810 compliant surface. *J. Fluid Mech.* **197**, 201–240.
811 Shankar, V. & Kumaran, V. 2002 Stability of wall modes in fluid flow past a flexible surface. *Phys. Fluids*
812 **14**, 2324–2338.
813 Singer, B. A., Ferziger, J. H. & Reed, H. L 1989 Numerical simulations of transition in oscillatory plane
814 channel flow. *J. Fluid Mech.* **208**, 45–66.
815 Straatman, A. G., Khayat, R. E., Haj-Qasem, E. & Steinman, D. A. 2002 On the hydrodynamic stability
816 of pulsatile flow in a plane channel. *Phys. Fluids* **14**, 1938–1944.
817 Tsigklifis, K. & Lucey, A. D. 2017 Asymptotic stability and transient growth in pulsatile Poiseuille flow
818 through a compliant channel. *J. Fluid Mech.* **820**, 370–399.
819 Womersley, J. R. 1955 Method for the calculation of velocity, rate of flow and viscous drag in arteries
820 when pressure gradient is known. *J. Physiol* **127**, 553–563.
821 Xu, D., Song, B. & Avila, M. 2021 Non-modal transient growth of disturbances in pulsatile and oscillatory
822 pipe flows. *J. Fluid Mech.* **907**, R5.
823 Xu, D., Varshney, A., Ma, X., Song, B., Riedl, M., Avila, M. & Hof, B. 2020 Nonlinear hydrodynamic
824 instability and turbulence in pulsatile flow. *Proc. Natl Acad. Sci. USA* **117**, 11233–11239.